JM PAPERS

The motion of a thin drop on an elastic sheet

Zhixuan Li[1] and **Weiqing Ren**[1]

[1]Department of Mathematics, National University of Singapore, Singapore 119076, Republic of Singapore
Corresponding author: Weiqing Ren, matrw@nus.edu.sg

We investigate the motion of a thin liquid drop on a pre-stretched, highly bendable elastic sheet. Under the lubrication approximation, we derive a system of fourth-order partial differential equations, along with appropriate boundary and contact line conditions, to describe the evolution of the fluid interface and the elastic sheet. Extending the classical analysis of Cox and Voinov, we perform a four-region matched asymptotic analysis of the model in the limit of small slip length. The central result is an asymptotic relation for the contact line speed in terms of the apparent contact angles. We validate the relation through numerical simulations. A key implication of this result is that a soft substrate retards drop spreading but enhances receding, compared to the dynamics on a rigid substrate. The relation remains valid across a wide range of bending modulus, despite the distinguished limit assumed in the analysis.

1. Introduction

Wetting phenomena are ubiquitous in nature and play a crucial role in numerous industrial applications, including oil recovery (Tangparitkul *et al.* 2018), inkjet printing (Park & Moon 2006), microfluidics manipulation (Stone, Stroock & Ajdari 2004) and coating processes (Kajiya *et al.* 2014). A fundamental problem in wetting dynamics is the motion of the contact line, where the interface between two immiscible fluids meets a solid substrate, and one fluid displaces the other (De Gennes 1985; Bonn *et al.* 2009). A well-known paradox arises in hydrodynamic models: imposing the conventional no-slip condition at the solid surface leads to an unphysical, non-integrable singularity in the viscous dissipation at the moving contact line (Huh & Scriven 1971; Snoeijer & Andreotti 2013). To resolve this issue, various models have been proposed over the past decades, including molecular kinetic models, molecular dynamic models, phase field models, and

hydrodynamic models with modified boundary conditions; see the literature reviews in Ren & E (2007) and Ren, Trinh & E (2015). Among these models, a particularly simple and widely used approach is the Navier slip model, which introduces a small region of length λ_0 where slip of the fluids occurs. This regularises the singularity and allows for a consistent description of contact line motion.

In their theoretical studies, Cox (1986) and Voinov (1977) conducted a three-region matched asymptotic analysis in the limit of small slip length $\lambda = \lambda_0/L \ll 1$, where λ_0 is the physical slip length, and L is a characteristic length scale of the flow. For simplicity, we will hereafter refer to the dimensionless parameter λ as the slip length. The three regions are as follows. (i) The outer region, located at a distance of O(1) from the contact line, where fluid slip is negligible and the apparent contact angle θ_{app} is defined. (ii) The inner region, located at a distance O(λ) from the contact line, where slip occurs and the microscopic contact angle θ_m is defined; the microscopic contact angle typically differs from the apparent one at a moving contact line. (iii) The intermediate region, which spans distances between O(λ) and O(ϵ) from the contact line. This transition zone connects the inner and outer regions, and captures the bending of the fluid interface. Here, the intermediate length scale

$$\epsilon = \frac{1}{|\log \lambda|} \tag{1.1}$$

satisfies $\lambda \ll \epsilon \ll 1$ and tends to zero as $\lambda \to 0$. We refer to Sibley, Nold & Kalliadasis (2015) for a review of the Cox–Voinov theory and its underlying asymptotic structure. The main result of the asymptotic analysis is a relation between the contact line speed and the apparent contact angle. This relation has been successfully applied to many wetting problems (Hocking 1977; Hocking & Rivers 1982; Cox 1986). For thin liquid drops, the lubrication approximation has been used to derive simplified models (Hocking 1983; Savva & Kalliadasis 2009; Ren *et al.* 2015).

The Cox–Voinov theory has been widely used to describe contact line motion. Its application requires proper identification of the relevant length scales. The slip length is not determined within the theory itself; rather, it must be prescribed, for example, through calibration against experimental measurements or molecular-scale models. In addition, the apparent contact angle defined in the outer region can be problem-dependent. For spreading drops, for instance, it is commonly defined by fitting a circular arc to the fluid interface, then calculating the angle that it makes with the substrate.

In contrast to the asymptotic matching between different scales employed by Voinov (1977) and Cox (1986), Snoeijer (2006) and Chan *et al.* (2020) adopted an alternative approach in which the free surface is treated as a perturbation around a straight wedge. Based on the wedge flow solution (Huh & Scriven 1971), they derived the 'generalised lubrication' equation, which provides a description of the interface profile at small capillary numbers. This method avoids the need to distinguish between different asymptotic regions, and the resulting generalised lubrication equation remains valid even for large interface slopes.

In recent years, the field of elastocapillarity – the interplay between elasticity and capillarity – has attracted much research attention. Wetting problems in this context, often referred to as soft wetting, have been considered in a large body of works; see Bico, Reyssat & Roman (2018) and Andreotti & Snoeijer (2020). Soft wetting differs from classical wetting due to the deformability of the substrate. In this setting, the substrate can deform in response to fluid pressure, viscous stress, and capillary forces exerted at the contact line. Notably, a wetting ridge forms at the contact line on a (visco)elastic solid (Jerison *et al.* 2011; Style & Dufresne 2012; Pandey *et al.* 2020), and is associated

with interesting phenomena such as viscoelastic braking (Shanahan 1988) and stick-slip motion of the contact line (Kajiya *et al.* 2013; Karpitschka *et al.* 2015). More recently, the dynamics of thin liquid films on (visco)elastic substrates has been studied (Charitatos & Kumar 2020; Henkel, Snoeijer & Thiele 2021; Tamim & Bostwick 2021, 2023). These works typically employ the lubrication approximation to derive reduced models, and use either a sharp interface or a precursor film approach to model the moving contact line. Various factors affecting the spreading dynamics have been investigated, including fluid evaporation, Marangoni effects and substrate properties.

Among soft wetting problems, the wetting of thin elastic sheets has been an active subject of research. For example, a drop deposited on an ultrathin sheet can induce wrinkling, a phenomenon first reported by Huang *et al.* (2007). The equilibrium properties of this drop–sheet system, including the wrinkle extent and wavelength, have been studied in detail (Davidovitch *et al.* 2011; King *et al.* 2012; Schroll *et al.* 2013; Davidovitch & Vella 2018). Following the work of Py *et al.* (2007) on capillary folding, subsequent studies have been carried out to establish the criteria for the reopening of an elastic sheet upon drop evaporation (Péraud & Lauga 2014; Brubaker & Lega 2015; Li & Ren 2024*a*,*b*). Static interface profiles for contact lines on elastic membranes were studied in Zhang, Yao & Ren (2020). In addition, Bradley investigated the spontaneous transport of drops on elastic sheets through a mechanism called 'bendotaxis' (Bradley *et al.* 2019). Onsager's variational principle (Zhang & Qian 2022) or non-equilibrium thermodynamics (Yao, Zhang & Ren 2023) has been used to develop models to further investigate the mechanisms underlying this spontaneous transport.

Despite the extensive literature on soft wetting, a theoretical analysis of contact line motion on elastic sheets remains lacking. In this work, we consider the motion of a thin drop on an elastic sheet. The sheet is thin, stretched, highly bendable, and simply supported in the far field. The liquid height and the sheet deformation are assumed to be small, allowing us to apply the lubrication approximation; see e.g. Hocking (1983), Ehrhard & Davis (1991) and Oron, Davis & Bankoff (1997). Our main objective is to derive a relation – analogous to the Cox–Voinov relation – between the contact line speed and measurable quantities such as the drop radius and the apparent contact angles. Compared with classical wetting, our problem is complicated by the substrate deformability and its coupling with the fluid. The elastic sheet bends moderately beneath the drop but exhibits sharp bending near the contact line. This localised bending occurs on the dimensionless length scale

$$l = \sqrt{C_b/\gamma}/L \ll 1, \tag{1.2}$$

where C_b is the bending modulus, and γ is the sheet tension. This scale arises from the balance between the bending resistance force and the tension force. We expect that the sheet bending on this scale influences the contact line dynamics. As a consequence of the sharp bending, we introduce two apparent contact angles: the angle α_{app} that the fluid interface makes with the horizontal plane, and the angle β_{app} that the sheet makes with the horizontal plane, both measured at a distance O(1) from the contact line; see figure 1. We expect that both angles, rather than $\theta_{app} = \alpha_{app} - \beta_{app}$, the angle between the interface and the sheet alone, contribute to determining the contact line dynamics.

We extend the classical Cox–Voinov analysis to account for the sheet bending. We consider the distinguished limit in which the capillary number is $Ca = O(\epsilon)$ and the bending length is $l = O(\epsilon)$, where ϵ is defined in (1.1). A bending region of size O(ϵ) is introduced where the sheet deformation plays a dominant role. We systematically solve the interface profile and the sheet deformation in the outer, bending and inner regions, and use the intermediate region to connect the solutions in the bending and inner regions. Through this matched asymptotic analysis, we derive a relation that expresses the contact
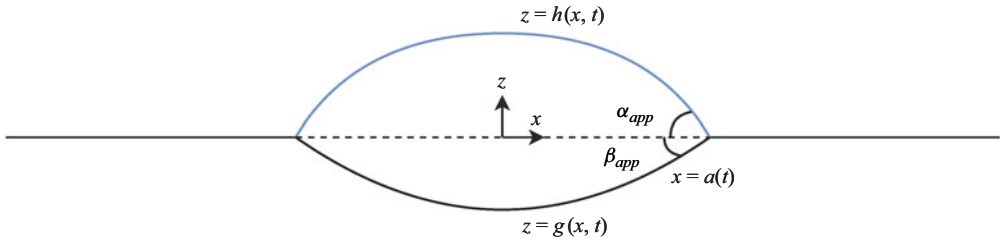
Figure 1. Spreading of a thin liquid drop on an elastic sheet. The fluid interface is represented by $z = h(x, t)$, the sheet by $z = g(x, t)$, and the contact line position by $x = a(t)$. The apparent contact angles α_{app} and β_{app} are defined relative to the horizontal plane for the fluid interface and the sheet, respectively. In the configuration shown, $\alpha_{app} > 0$ and $\beta_{app} < 0$.

line speed in terms of the apparent contact angles α_{app} and β_{app}:

$$3\, Ca\, \epsilon^{-1} \dot{a} \sim \left(\alpha_{app} - \frac{\sqrt{\gamma_1}}{\sqrt{\gamma_1} + \sqrt{\gamma_2}} \beta_{app} \right)^3 - \theta_Y^3, \tag{1.3}$$

where $\dot{a}$ is the contact line speed, θ_Y is the equilibrium contact angle, and γ_1, γ_2 are the effective tensions in the wet and dry parts of the sheet, respectively. This relation reveals that the contact line dynamics is significantly influenced by the substrate rigidity: softer or less stretched sheets lead to retarded spreading and enhanced receding, as confirmed by numerical simulations. Furthermore, despite the assumption $l = O(\epsilon)$ in the analysis, the relation (1.3) is independent of the bending modulus. Our numerical simulations further confirm that the contact line dynamics is insensitive to the bending length, and that the relation holds even for extremely bendable sheets with l as small as $O(\epsilon^2)$.

The rest of this paper is organised as follows. In § 2, we derive a system of fourth-order equations, together with appropriate boundary and contact line conditions, that govern the evolution of the fluid interface and the elastic sheet. In § 3, we perform a four-region matched asymptotic analysis of the model, and derive a relation describing the contact line motion on an elastic sheet. In § 4, we validate the theoretical results through numerical simulations, and examine retarded spreading, enhanced receding and long-time dynamics. Finally, we conclude the paper in § 5.

2. A thin-film model

We begin with a hydrodynamics model for the drop–sheet system. Consider a two-dimensional liquid drop surrounded by air and sitting on a one-dimensional elastic sheet; see figure 1. The interfacial tension coefficient for the liquid–air interface is γ_3. For simplicity, we assume that the drop is symmetric with respect to $x = 0$, and that the contact line is located at $x = \pm a(t)$. We represent the liquid–air interface by the height function $z = h(x, t)$, $-a(t) \leqslant x \leqslant a(t)$, and the sheet profile by the height function $z = g(x, t)$, $-\infty < x < \infty$. The liquid is assumed to be incompressible and Newtonian, with dynamical viscosity η. Its dynamics is modelled by the stationary Stokes equations. The viscosity of the surrounding air is assumed to be negligible, and its influence on the liquid is neglected. The elastic sheet is modelled using the Willmore bending energy with bending modulus C_b. Motivated by the experimental set-ups in Huang *et al.* (2007) and King *et al.* (2012), we assume that the sheet has a very large stretching modulus, is nearly inextensible, and is uniformly stretched with a pre-stress $\sigma_{pre} > 0$. We then define

the effective tensions as

$$\gamma_i = \gamma_{i,o} + \sigma_{pre}, \quad i = 1, 2, \tag{2.1}$$

where $\gamma_{i,o}$, $i = 1, 2$ are the interfacial tension coefficients of the liquid–sheet and air–sheet interfaces, respectively. We refer to Yao *et al.* (2023) for a complete description and the derivation of the hydrodynamics model.

In the following, we consider a thin liquid film that is symmetric about $x = 0$, and restrict our attention to the half-domain $x \geqslant 0$. Let L denote the characteristic film radius, and U the characteristic contact line velocity. We assume that the film height is of order δL, where $\delta \ll 1$ is a small parameter. Furthermore, we assume that the slope of the film height is $\partial h / \partial x = O(\delta)$. Similarly, we assume $g = O(\delta L)$ and $\partial g / \partial x = O(\delta)$. We introduce the rescalings

$$(X, A) = \frac{(x, a)}{L}, \quad (Z, H, G) = \frac{(z, h, g)}{\delta L}, \quad T = \frac{t}{L/U}, \tag{2.2}$$

with the dimensionless variables marked by uppercase letters. We also introduce the dimensionless parameters

$$Ca = \frac{3\eta U}{\gamma_3 \delta^3}, \quad \tilde{\gamma}_i = \frac{\gamma_i \delta^3}{3\eta U}, \quad \tilde{C}_b = \frac{C_b \delta^3}{3\eta U L^2}. \tag{2.3}$$

Following the standard procedure (see e.g. Oron *et al.* 1997), we derive from the hydrodynamics model the evolution equations for the interface height $Z = H(X, T)$ and the sheet profile $Z = G(X, T)$:

$$\partial_T (H - G) + \partial_X F = 0, \quad 0 < X < A(T), \tag{2.4a}$$

$$F = \frac{1}{Ca}(H - G)^2 (H - G + \lambda) \, \partial_X^3 H, \tag{2.4b}$$

$$\tilde{C}_b \, \partial_X^4 G = \begin{cases} \tilde{\gamma}_1 \, \partial_{XX} G + Ca^{-1} \, \partial_{XX} H, & 0 < X < A(T), \\ \tilde{\gamma}_2 \, \partial_{XX} G, & A(T) < X. \end{cases} \tag{2.4c}$$

The boundary conditions are as follows. At the origin, symmetry conditions are imposed:

$$\begin{cases} \partial_X H = \partial_X^3 H = 0, \\ \partial_X G = \partial_X^3 G = 0, \end{cases} \quad \text{at } X = 0. \tag{2.5}$$

At the far field, we assume simply supported conditions:

$$G = \partial_{XX} G = 0 \quad \text{at } X = +\infty. \tag{2.6}$$

Additionally, the kinematic compatibility condition requires that the liquid–air interface and the elastic sheet meet at the moving contact line:

$$H(A(T), T) = G(A(T), T). \tag{2.7}$$

We note that (2.4) has the same form as the usual thin-film equation with slip, except that the liquid height is now given by $H - G$. Meanwhile, (2.4c) is a fourth-order linear beam equation with an additional second-order tension term.

2.1. *Thermodynamics and contact line conditions*

Based on (2.4)–(2.7), we now derive appropriate contact line conditions following the principles of non-equilibrium thermodynamics (Ren, Hu & E 2010; Ren & E 2011).

We start with the system total energy under the lubrication approximation:

$$
\begin{aligned}
\mathcal{E} &= \mathcal{E}_s + \mathcal{E}_b, \\
\mathcal{E}_s &= \frac{1}{Ca} \int_0^{A(t)} \left(1 + \frac{\delta^2}{2} |\partial_X H|^2 \right) \mathrm{d}X \\
&\quad + \tilde{\gamma}_1 \int_0^{A(t)} \left(1 + \frac{\delta^2}{2} |\partial_X G|^2 \right) \mathrm{d}X + \tilde{\gamma}_2 \int_{A(t)}^{X_r} \left(1 + \frac{\delta^2}{2} |\partial_X G|^2 \right) \mathrm{d}X, \\
\mathcal{E}_b &= \frac{\tilde{C}_b}{2} \int_0^{X_r} \delta^2 |\partial_{XX} G|^2 \, \mathrm{d}X,
\end{aligned}
\tag{2.8}
$$

where $\mathcal{E}_s$ denotes the total interfacial energy, and $\mathcal{E}_b$ is the bending energy of the elastic sheet. To avoid an infinite interfacial energy, here we apply the far-field condition (2.6) at the fixed boundary $X = X_r$ (instead of $X = +\infty$) to suppress any energy dissipation at this point. (It is more rigorous to deal with a finite energy, although the derivation in this subsection remains valid, at least formally, with $X_r = \infty$.)

Next, we compute the energy dissipation rate. For the bending energy, we have

$$
\begin{aligned}
\frac{\mathrm{d}\mathcal{E}_b}{\mathrm{d}T} &= \delta^2 \tilde{C}_b \left(-[\![\partial_{XX} G]\!] \cdot \partial_{XT} G + [\![\partial_X^3 G]\!] \cdot \partial_T G \right)_{X=A(T)} \\
&\quad + \delta^2 \frac{\tilde{C}_b}{2} [\![|\partial_{XX} G|^2]\!] \, \dot{A}(T) \\
&\quad + \delta^2 \tilde{C}_b \left\{ \int_0^{A(T)} \partial_X^4 G \cdot \partial_T G \, \mathrm{d}X + \int_{A(T)}^{X_r} \partial_X^4 G \cdot \partial_T G \, \mathrm{d}X \right\},
\end{aligned}
\tag{2.9}
$$

where we have used the symmetry condition (2.5) at $X = 0$, and the far-field condition (2.6) at $X = X_r$. The symbol $[\![\cdot]\!]$ denotes the jump of a quantity across the contact line from $X = A(T)^-$ to $X = A(T)^+$.

The dissipation rate of the interfacial energy can be decomposed into three contributions:

$$
\begin{aligned}
\frac{\mathrm{d}\mathcal{E}_s}{\mathrm{d}T} &= \dot{\mathcal{E}}_{s,1} + \dot{\mathcal{E}}_{s,2} + \dot{\mathcal{E}}_{s,3}, \\
\dot{\mathcal{E}}_{s,1} &= \delta^2 \left\{ \frac{1}{Ca} \partial_X H \cdot \partial_T H + (\tilde{\gamma}_1 - \tilde{\gamma}_2) \, \partial_X G \cdot \partial_T G \right\}_{X=A(T)}, \\
\dot{\mathcal{E}}_{s,2} &= \dot{A}(T) \left\{ \frac{1}{Ca} \left(1 + \frac{\delta^2}{2} |\partial_X H|^2 \right) + (\tilde{\gamma}_1 - \tilde{\gamma}_2) \left(1 + \frac{\delta^2}{2} |\partial_X G|^2 \right) \right\}_{X=A(T)}, \\
\dot{\mathcal{E}}_{s,3} &= -\delta^2 \left\{ \frac{1}{Ca} \int_0^{A(T)} \partial_{XX} H \cdot \partial_T H \, \mathrm{d}X \right. \\
&\quad \left. + \tilde{\gamma}_1 \int_0^{A(T)} \partial_{XX} G \cdot \partial_T G \, \mathrm{d}X + \tilde{\gamma}_2 \int_{A(T)}^{X_r} \partial_{XX} G \cdot \partial_T G \, \mathrm{d}X \right\}.
\end{aligned}
\tag{2.10}
$$

We take the time derivative of the kinematic compatibility condition (2.7) and use the resulting relation to simplify $\dot{\mathcal{E}}_{s,1}$ and $\dot{\mathcal{E}}_{s,2}$. After some manipulation, we obtain

$$
\dot{\mathcal{E}}_{s,1} + \dot{\mathcal{E}}_{s,2} = \delta^2 \left\{ \left(\frac{1}{Ca} \partial_X H + (\tilde{\gamma}_1 - \tilde{\gamma}_2) \partial_X G \right) \partial_T G \right\}_{X=A(T)}
$$
$$
+ \frac{\delta^2}{Ca} \dot{A}(T) \left\{ \frac{1}{2} \Theta_Y^2 - \frac{1}{2} |\partial_X H - \partial_X G|^2 \right\}_{X=A(T)} + \mathrm{O}\left(\delta^4\right), \tag{2.11}
$$

where Θ_Y is the rescaled Young's angle defined via Young's relation (Young 1805)

$$
Ca\,(\tilde{\gamma}_2 - \tilde{\gamma}_1) = 1 - \frac{\delta^2}{2} \Theta_Y^2, \tag{2.12}
$$

the right-hand side being the small-angle expansion of the cosine function. To handle $\dot{\mathcal{E}}_{s,3}$, we use the thin film (2.4), which leads to the identity

$$
\int_0^{A(T)} \partial_{XX} H \cdot \partial_T H \,\mathrm{d}X
$$
$$
= \int_0^{A(T)} \partial_{XX} H \cdot \partial_T G \,\mathrm{d}X + \int_0^{A(T)} \frac{1}{Ca} (H - G)^2 (H - G + \lambda) \left|\partial_X^3 H\right|^2 \mathrm{d}X, \tag{2.13}
$$

where we have used integration by parts and the fact that $F = 0$ at $X = 0$ and $X = A(T)$.

Finally, we combine (2.9), (2.10), (2.11) and (2.13), and apply the sheet (2.4c) to obtain the dissipation rate for the total energy:

$$
\frac{\mathrm{d}\mathcal{E}}{\mathrm{d}T} = -\frac{\delta^2}{Ca^2} \int_0^{A(T)} (H - G)^2 (H - G + \lambda) \left|\partial_X^3 H\right|^2 \mathrm{d}X \tag{2.14a}
$$

$$
- \delta^2 \tilde{C}_b \left\{ [\![\partial_{XX} G]\!] \cdot \partial_{XT} G \right\}_{X=A(T)} + \delta^2 \frac{\tilde{C}_b}{2} [\![|\partial_{XX} G|^2]\!] \, \dot{A}(T) \tag{2.14b}
$$

$$
+ \delta^2 \left\{ \left(\frac{1}{Ca} \partial_X H + (\tilde{\gamma}_1 - \tilde{\gamma}_2) \partial_X G + \tilde{C}_b [\![\partial_X^3 G]\!] \right) \partial_T G \right\}_{X=A(T)} \tag{2.14c}
$$

$$
+ \frac{\delta^2}{Ca} \left\{ \frac{1}{2} \Theta_Y^2 - \frac{1}{2} |\partial_X H - \partial_X G|^2 \right\}_{X=A(T)} \dot{A}(T) \tag{2.14d}
$$

$$
+ \mathrm{O}\left(\delta^4\right). \tag{2.14e}
$$

This equation shows that the energy dissipation consists of dominant terms of $\mathrm{O}(\delta^2)$ and some higher-order contributions. Among the dominant terms, the term in (2.14a) arises from the dynamics of the bulk fluid, while the remaining terms (2.14b)–(2.14d) are associated with the contact line dynamics. Under the physical constraint $H - G \geqslant 0$ for $0 < X < A(T)$, the term in (2.14a) is always non-positive, and the thin-film motion always dissipates energy. To ensure that the total system energy decays, at least to leading order in $\mathrm{O}(\delta^2)$, we will derive and impose appropriate conditions at the moving contact line. For this purpose, we have written the contact-line-related terms in the form of a product of a generalised force and a generalised flux. Next, we examine these terms one by one.

In the first term of (2.14b), the generalised force is the jump in the curvature across the contact line, while the generalised flux is the rate of sheet rotation about the contact line. We assume that the sheet rotation here does not induce any energy change, so we set the generalised force to zero, and obtain a continuity condition for the curvature:

$$
[\![\partial_{XX} G]\!] = 0 \quad \text{at } X = A(T). \tag{2.15}
$$

The second term of (2.14*b*) vanishes given the continuity of the sheet curvature established above. Therefore, this term does not contribute to the energy dissipation.

In (2.14*c*), the generalised force is the resultant vertical force acting at the contact line, while the generalised flux is the vertical velocity of the sheet at the contact line. (Note that this is not a material velocity, however.) We assume that the sheet motion at the contact line alone does not induce any energy change. This yields the following balance condition at the contact line:

$$\frac{1}{Ca} \, \partial_X H + (\tilde{\gamma}_1 - \tilde{\gamma}_2) \, \partial_X G = -\tilde{C}_b \, [\![\partial_X^3 G]\!] \quad \text{at } X = A(T). \tag{2.16}$$

In (2.14*d*), the generalised force is an approximation of the unbalanced Young stress in the horizontal direction, while the generalised flux is the contact line speed. Assuming a linear constitutive relation between the two, we obtain

$$\frac{1}{2} \, |\partial_X H - \partial_X G|^2 - \frac{1}{2} \Theta_Y^2 = Ca \, \tilde{\mu}_\Lambda \, \dot{A}(T). \tag{2.17}$$

Here, $\tilde{\mu}_\Lambda > 0$ is a dimensionless friction coefficient, representing the resistance to contact line motion. It is a physical parameter whose value in general depends on fluid properties, substrate roughness and microscopic characteristics.

To conclude this section, we have derived a model for the motion of a thin film on an elastic sheet based on the lubrication approximation. The primary unknowns of this model are the liquid–air interface profile $z = h(x, t)$ and the elastic sheet profile $z = g(x, t)$, with the contact line located at $x = a(t)$. The dimensionless governing equations are summarised below. For better readability, we revert to lowercase variables and omit overhead tildes:

$$\partial_t \, (h - g) + Ca^{-1} \, \partial_x \left((h - g)^2 \, (h - g + \lambda) \, \partial_x^3 h \right) = 0, \quad 0 < x < a(t), \tag{2.18a}$$

$$C_b \, \partial_x^4 g - \gamma_1 \, \partial_{xx} g = Ca^{-1} \, \partial_{xx} h, \quad 0 < x < a(t), \tag{2.18b}$$

$$C_b \, \partial_x^4 g - \gamma_2 \, \partial_{xx} g = 0, \quad a(t) < x. \tag{2.18c}$$

The boundary conditions are

$$\partial_x h = \partial_x^3 h = 0 \quad \text{at } x = 0, \tag{2.19a}$$

$$\partial_x g = \partial_x^3 g = 0 \quad \text{at } x = 0, \tag{2.19b}$$

$$g = \partial_{xx} g = 0 \quad \text{at } x = +\infty. \tag{2.19c}$$

The contact line conditions at $x = a(t)$ are

$$[\![g]\!] = [\![\partial_x g]\!] = [\![\partial_{xx} g]\!] = 0, \tag{2.20a}$$

$$Ca^{-1} \, \partial_x h + (\gamma_1 - \gamma_2) \, \partial_x g = -C_b \, [\![\partial_x^3 g]\!], \tag{2.20b}$$

$$\frac{1}{2} \, |\partial_x h - \partial_x g|^2 - \frac{1}{2} \theta_Y^2 = Ca \, \mu_\Lambda \, \dot{a}(t), \tag{2.20c}$$

$$h(a(t), t) = g(a(t), t). \tag{2.20d}$$

In this model, the total energy of the system changes as

$$\frac{d\mathcal{E}}{dt} = -\frac{\delta^2}{Ca^2} \int_0^{a(t)} (h - g)^2 \, (h - g + \lambda) \, \left|\partial_x^3 h\right|^2 dx - \delta^2 \mu_\Lambda \, |\dot{a}(t)|^2 + O\left(\delta^4\right), \tag{2.21}$$

where the first and second terms on the right-hand side represent the dissipation rates due to the thin-film motion and the contact line motion, respectively.

3. Asymptotic analysis

The classical Cox–Voinov theory describes the spreading (or receding) rate of a liquid film on a rigid substrate in the limit of small slip length $\lambda \ll 1$, and capillary number $Ca = \mathrm{O}(\epsilon)$, where ϵ is defined in (1.1). The central result can be stated as

$$3\, Ca\, \epsilon^{-1}\, \dot{a}(t) \sim \theta_{app}^3 - \theta_Y^3, \tag{3.1}$$

where θ_{app} is the apparent contact angle that the interface makes with the substrate when viewed at a distance of $\mathrm{O}(1)$ from the contact line. This relation has been verified through previous experimental and theoretical works; see e.g. Hocking & Rivers (1982), Cox (1986) and Ngan & Dussan (1989). The small capillary number assumption $Ca = \mathrm{O}(\epsilon)$ is essential for the applicability of the Cox–Voinov theory. In this regime, the interface is only weakly curved near the contact line, and the flow can be treated as a perturbation around the wedge solution (Huh & Scriven 1971), which forms the basis of the Cox–Voinov analysis and its extensions. When $Ca \sim 1$, however, the interface may develop a cusp-like structure near the contact line (Kamal *et al.* 2019). In such cases, the wedge flow approximation is no longer valid, and a more detailed description of the interface is required.

We now set up the formulation to extend the Cox–Voinov analysis to the case where the substrate is an elastic sheet. The governing equations for the dynamics of the fluid interface and the sheet are given in (2.18)–(2.20). We consider the limit of small slip length $\lambda \ll 1$, with the scaling $Ca = Ca^* \epsilon$, where Ca^* is an $\mathrm{O}(1)$ constant. Since the effective tensions γ_i ($i = 1, 2$) are of the same order as γ_3, we write $\gamma_i = \gamma_i^*/\epsilon$, where the γ_i^* are $\mathrm{O}(1)$ constants. Additionally, we consider a highly bendable sheet with bending modulus $C_b = C_b^* \epsilon$, where C_b^* is an $\mathrm{O}(1)$ constant. In this regime, the corresponding (dimensionless) bending length $l_i = \sqrt{C_b^*/\gamma_i^*}\, \epsilon$ is consistent with typical experimental parameters (e.g. Huang *et al.* 2007) and is therefore of practical interest. (For illustration, consider a slip length on the molecular scale of 1 nm and drop radius 1 mm, giving $\lambda = 10^{-6}$ and $\epsilon \approx 0.072$. For a polystyrene sheet with Young's modulus 3.4 GPa, thickness 200 nm, Poisson ratio 1/3, and interfacial tension 30 nN m^{-1}, the resulting dimensionless bending length is $l \approx 0.0093 \lesssim \epsilon$.)

We note that the $\mathrm{O}(1)$ parameter Ca^* has no fundamental influence on the contact line dynamics, nor is it essential for the mathematical analysis. To keep the exposition simple, we will restrict to the specific case $Ca^* = 1$ in the rest of this section. The general case can be recovered from this specific one by straightforward rescaling. Below, we summarise the rescaled governing equations, with all asterisks dropped for notational simplicity:

$$\epsilon\, \partial_t\, (h - g) + \partial_x \left((h - g)^2\, (h - g + \lambda)\, \partial_x^3 h \right) = 0, \quad 0 < x < a(t), \tag{3.2a}$$

$$C_b \epsilon^2\, \partial_x^4 g - \gamma_1\, \partial_{xx} g = \partial_{xx} h, \quad 0 < x < a(t), \tag{3.2b}$$

$$C_b \epsilon^2\, \partial_x^4 g - \gamma_2\, \partial_{xx} g = 0, \quad a(t) < x. \tag{3.2c}$$

The conditions at the moving contact line $x = a(t)$ are

$$[\![g]\!] = [\![\partial_x g]\!] = [\![\partial_{xx} g]\!] = 0, \tag{3.3a}$$

$$\partial_x h + (\gamma_1 - \gamma_2)\, \partial_x g = -C_b \epsilon^2\, [\![\partial_x^3 g]\!], \tag{3.3b}$$
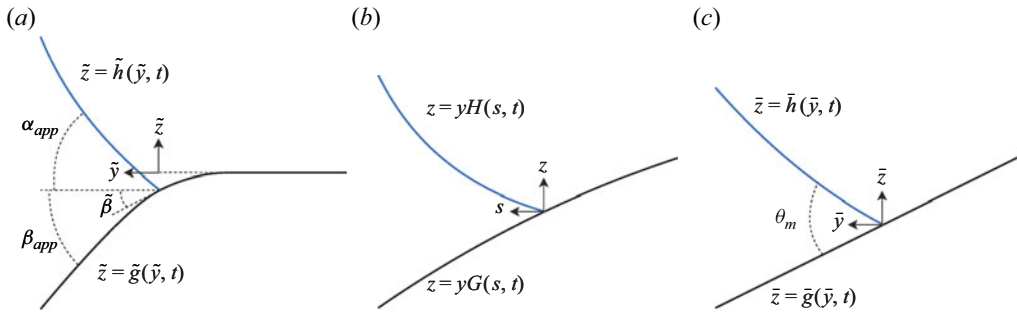
Figure 2. (*a*) Bending region, viewed at a distance O(ϵ) from the contact line, with coordinates ($\tilde{y}, \tilde{z}$); in this region, $\tilde{\beta}$ denotes the slope of the sheet at the contact line. (*b*) Intermediate region, with coordinates (s, z), where $0 < s = \epsilon \log y + 1 < \epsilon \log \epsilon + 1$. (*c*) Inner region, viewed at a distance O(λ) from the contact line, with coordinates ($\tilde{y}, \tilde{z}$); here, θ_m is the microscopic contact angle.

$$\frac{1}{2} |\partial_x h - \partial_x g|^2 - \frac{1}{2}\theta_Y^2 = \epsilon \mu_\Lambda \dot{a}(t), \tag{3.3c}$$

$$h(a(t), t) = g(a(t), t). \tag{3.3d}$$

The symmetry and far-field boundary conditions remain the same as in (2.19).

The outline of our analysis is illustrated in figures 1 and 2. We perform the analysis in four regions: the outer region (figure 1), the bending region (figure 2*a*), the inner region (figure 2*c*) and the intermediate region (figure 2*b*). These analyses are carried out in §§ 3.1–3.4. In § 3.5, we match the solutions in the different regions, and derive an effective model for the contact line speed, analogous to the Cox–Voinov relation (3.1).

3.1. *Outer region*

We expand the contact line speed in powers of ϵ:

$$\dot{a}(t) = \dot{a}_0(t) + \epsilon \dot{a}_1(t) + \cdots, \tag{3.4}$$

where $\epsilon \dot{a}_1$ is o(1) for the expansion to be well ordered. Similarly, we expand the profiles

$$\begin{aligned} h(x, t) &= h_0(x, t) + \epsilon h_1(x, t) + \cdots, \\ g(x, t) &= g_0(x, t) + \epsilon g_1(x, t) + \cdots. \end{aligned} \tag{3.5}$$

Substituting these expansions into the governing equation (3.2), we obtain the leading-order equations for h_0 and g_0:

$$\partial_x \left((h_0 - g_0)^3 \partial_x^3 h_0 \right) = 0, \quad 0 < x < a(t), \tag{3.6a}$$

$$-\gamma_1 \partial_{xx} g_0 = \partial_{xx} h_0, \quad 0 < x < a(t), \tag{3.6b}$$

$$\partial_{xx} g_0 = 0, \quad a(t) < x. \tag{3.6c}$$

The leading-order boundary conditions are given by

$$\begin{aligned} \partial_x h_0 &= \partial_x^3 h_0 = 0 \quad \text{at } x = 0, \\ \partial_x g_0 &= 0 \quad \text{at } x = 0, \\ g_0 &= 0 \quad \text{at } x = +\infty, \end{aligned} \tag{3.7}$$

and the leading-order contact line conditions are

$$\llbracket g_0 \rrbracket = 0,$$
$$h_0(a(t), t) = g_0(a(t), t). \tag{3.8}$$

To solve this system, we first deduce from (3.6c) and the far-field condition that $g \equiv 0$ when $a(t) \leqslant x$. We then solve (3.6a) and (3.6b) with the boundary and contact line conditions. To fully determine the solution, we need to impose the conservation of the liquid volume V. The leading-order solution is then given by

$$h_0(x, t) = \frac{p_0}{2}(a^2 - x^2), \quad 0 \leqslant x \leqslant a(t),$$

$$g_0(x, t) = \begin{cases} \dfrac{p_0}{2\gamma_1}(x^2 - a^2), & 0 \leqslant x \leqslant a(t), \\ 0, & a(t) < x, \end{cases} \tag{3.9}$$

where we have introduced the pressure p_0 for notational convenience:

$$p_0 = \frac{3V}{a^3(1 + \gamma_1^{-1})}. \tag{3.10}$$

We note that this solution automatically satisfies the higher-order boundary conditions $\partial_x^3 g_0 = 0$ at $x = 0$, and $\partial_x^2 g_0 = 0$ at $x = +\infty$. For later use, we compute the leading-order film thickness:

$$h_0 - g_0 = \frac{3V}{2a^3}(a^2 - x^2). \tag{3.11}$$

The next-order equations from (3.2) are

$$\partial_t (h_0 - g_0) + \partial_x ((h_0 - g_0)^3 \partial_x^3 h_1) = 0, \quad 0 < x < a(t), \tag{3.12a}$$

$$-\gamma_1 \partial_{xx} g_1 = \partial_{xx} h_1, \quad 0 < x < a(t), \tag{3.12b}$$

$$\partial_{xx} g_1 = 0, \quad a(t) < x. \tag{3.12c}$$

The boundary conditions and contact line conditions take the same form as in (3.7) and (3.8), with h_0, g_0 replaced by h_1, g_1, respectively. As before, we have $g_1 \equiv 0$ when $a(t) \leqslant x$. To solve for h_1, we note that the dependence of the leading-order profiles h_0 and g_0 on time is only through $a(t)$. We integrate (3.12a) once with respect to x to obtain

$$\dot{a}_0 \frac{3V}{2a^4} x(x^2 - a^2) + \partial_x^3 h_1 \left[\frac{3V}{2a^3}(a^2 - x^2) \right]^3 = \text{const.} \tag{3.13}$$

We set the integration constant to zero, as it will yield a solution that matches the solutions in the other regions and is consistent with the numerical results. We proceed by further integrations. Using the boundary and contact line conditions as well as volume conservation, we can determine the next-order solutions:

$$h_1 = \dot{a}_0 \frac{a^4}{9V} \left\{ (a + x) \log (a + x) + (a - x) \log (a - x) - 2a \log 2a + \frac{3}{2a}(a^2 - x^2) \right\}, \tag{3.14a}$$

$$g_1 = \begin{cases} -\dfrac{1}{\gamma_1} h_1, & 0 \leqslant x \leqslant a(t), \\ 0, & a(t) < x. \end{cases} \tag{3.14b}$$

Before moving on, we introduce a moving coordinate system centred at the contact line. Let $x = a(t) - y$, where $y \leqslant a(t)$. In this coordinate system, the contact line is located at $y = 0$, and the governing equation for $h = h(y, t)$ becomes

$$\epsilon \left[\partial_t (h - g) + \dot{a}\, \partial_y (h - g) \right] + \partial_y \left((h - g)^2 (h - g + \lambda)\, \partial_y^3 h \right) = 0. \qquad (3.15)$$

The governing equations for $g = g(y, t)$ remain the same as in (3.2*b*)–(3.2*c*), but with ∂_x replaced by ∂_y. The symmetry conditions are now imposed at $y = a(t)$, the far-field conditions at $y = -\infty$, and the contact line conditions at $y = 0$. Their forms remain unchanged except for ∂_x being replaced by ∂_y. Near the contact line as $y \to 0^+$, the outer solutions in terms of y are

$$\begin{aligned}
h_0 &\sim \alpha_{app} y - \frac{\alpha_{app}}{2a} y^2, \\
h_1 &\sim \frac{\dot{a}_0}{\theta_{app}^2} \{ y \log y + (2 - \log 2a)\, y + \cdots \},
\end{aligned} \qquad (3.16)$$

and

$$\begin{aligned}
g_0 &\sim \beta_{app} y - \frac{\beta_{app}}{2a} y^2, \\
g_1 &\sim -\frac{1}{\gamma_1} h_1.
\end{aligned} \qquad (3.17)$$

Here, α_{app}, β_{app} and θ_{app} are the apparent contact angles for the interface, for the sheet, and between them, respectively. They are defined as

$$\begin{aligned}
\alpha_{app} &= \frac{\partial h_0(0, \cdot)}{\partial y} = \frac{3V}{a^2 \left(1 + \gamma_1^{-1}\right)}, \\
\beta_{app} &= \frac{\partial g_0(0, \cdot)}{\partial y} = -\frac{1}{\gamma_1} \frac{3V}{a^2 \left(1 + \gamma_1^{-1}\right)}, \\
\theta_{app} &= \alpha_{app} - \beta_{app} = \frac{3V}{a^2}.
\end{aligned} \qquad (3.18)$$

Next, we analyse the problem in the bending region.

3.2. *Bending region*

We rescale the variables in the bending region as $y = \epsilon \tilde{y}$, $h = \epsilon \tilde{h}$ and $g = \epsilon \tilde{g}$. The governing equations, written in terms of these variables, are

$$\epsilon^2\, \partial_t (\tilde{h} - \tilde{g}) + \epsilon \dot{a}\, \partial_{\tilde{y}} (\tilde{h} - \tilde{g}) + \partial_{\tilde{y}} \left[(\tilde{h} - \tilde{g})^2 (\tilde{h} - \tilde{g} + \lambda) \partial_{\tilde{y}}^3 \tilde{h} \right] = 0, \quad 0 < \tilde{y}, \qquad (3.19a)$$

$$C_b\, \partial_{\tilde{y}}^4 \tilde{g} - \gamma_1\, \partial_{\tilde{y}\tilde{y}} \tilde{g} = \partial_{\tilde{y}\tilde{y}} \tilde{h}, \quad 0 < \tilde{y}, \qquad (3.19b)$$

$$C_b\, \partial_{\tilde{y}}^4 \tilde{g} - \gamma_2\, \partial_{\tilde{y}\tilde{y}} \tilde{g} = 0, \quad \tilde{y} < 0. \qquad (3.19c)$$

To determine the appropriate boundary conditions as $\tilde{y} \to \pm\infty$, we rewrite the outer solutions (3.16) and (3.17) in terms of $\tilde{y}$, and arrange terms according to powers of ϵ.

Accordingly, we impose the far-field behaviour

$$\partial_{\tilde{y}}\tilde{h} \sim \alpha_{app} - \epsilon \frac{\alpha_{app}}{a}\tilde{y} + \epsilon \frac{\dot{a}_0}{\theta_{app}^2} \left(\log \tilde{y} + 3 + \log \epsilon - \log 2a + \cdots \right), \tag{3.20a}$$

$$\partial_{\tilde{y}}\tilde{g} \sim \beta_{app} - \epsilon \frac{\beta_{app}}{a}\tilde{y} - \epsilon \frac{\dot{a}_0}{\gamma_1 \theta_{app}^2} \left(\log \tilde{y} + 3 + \log \epsilon - \log 2a + \cdots \right), \tag{3.20b}$$

as $\tilde{y} \to +\infty$. In addition, from the outer solutions we have

$$\tilde{g} = \partial_{\tilde{y}}\tilde{g} = \partial_{\tilde{y}\tilde{y}}\tilde{g} = 0 \tag{3.21}$$

as $\tilde{y} \to -\infty$. At the contact line, we impose

$$[\![\tilde{g}]\!] = [\![\partial_{\tilde{y}}\tilde{g}]\!] = [\![\partial_{\tilde{y}\tilde{y}}\tilde{g}]\!] = 0,$$
$$\tilde{h}(0, \cdot) = \tilde{g}(0, \cdot). \tag{3.22}$$

We omit the contact line conditions (3.3b) and (3.3c) at this stage, as they are only relevant in the immediate vicinity of the contact line, i.e. the inner region.

We expand $\tilde{h}$ and $\tilde{g}$ in powers of ϵ:

$$\tilde{h}(\tilde{y}, t) \sim \tilde{h}_0(\tilde{y}, t) + \epsilon \tilde{h}_1(\tilde{y}, t) + \cdots,$$
$$\tilde{g}(\tilde{y}, t) \sim \tilde{g}_0(\tilde{y}, t) + \epsilon \tilde{g}_1(\tilde{y}, t) + \cdots. \tag{3.23}$$

The leading-order equations for $\tilde{h}_0$ and $\tilde{g}_0$ are

$$\partial_{\tilde{y}} \left[\left(\tilde{h}_0 - \tilde{g}_0 \right)^3 \partial_{\tilde{y}}^3 \tilde{h}_0 \right] = 0, \quad 0 < \tilde{y}, \tag{3.24a}$$

$$C_b \, \partial_{\tilde{y}}^4 \tilde{g}_0 - \gamma_1 \, \partial_{\tilde{y}\tilde{y}}\tilde{g}_0 = \partial_{\tilde{y}\tilde{y}}\tilde{h}_0, \quad 0 < \tilde{y}, \tag{3.24b}$$

$$C_b \, \partial_{\tilde{y}}^4 \tilde{g}_0 - \gamma_2 \, \partial_{\tilde{y}\tilde{y}}\tilde{g}_0 = 0, \quad \tilde{y} < 0. \tag{3.24c}$$

To solve these equations, we first consider (3.24a) for $\tilde{h}_0$. We integrate the equation once, set the constant of integration to zero, then integrate further and match the far-field condition in (3.20a), to obtain

$$\partial_{\tilde{y}}\tilde{h}_0 \equiv \alpha_{app}. \tag{3.25}$$

To solve (3.24b) and (3.24c), it is convenient to introduce

$$l_i = \sqrt{C_b/\gamma_i}, \quad i = 1, 2,$$
$$\tilde{y}_1 = \tilde{y}/l_1, \quad \tilde{y} \geqslant 0,$$
$$\tilde{y}_2 = \tilde{y}/l_2, \quad \tilde{y} \leqslant 0. \tag{3.26}$$

The general solutions to the fourth-order (3.24b) and (3.24c) are given by

$$\tilde{g}_0 = C_i^+ \, e^{\tilde{y}_i} + C_i^- \, e^{-\tilde{y}_i} + B_i \tilde{y} + A_i, \quad i = 1, 2, \tag{3.27}$$

where $i = 1, 2$ corresponds to the solution when $\tilde{y} > 0$ and $\tilde{y} < 0$, respectively. The eight constants are to be determined using the far-field conditions (3.20b) and (3.21), and the contact line conditions in (3.22). From the far-field conditions, we find that $C_1^+ = 0$, $C_2^- = 0$, $A_2 = B_2 = 0$ and $B_1 = \beta_{app}$. We then apply the continuity conditions in (3.22) to obtain

$$\tilde{g}_0 = \begin{cases} C_1^- \, e^{-\tilde{y}_1} + \beta_{app}\tilde{y} + A_1, & \tilde{y} \geqslant 0, \\ C_2^+ \, e^{\tilde{y}_2}, & \tilde{y} < 0, \end{cases} \tag{3.28}$$

1022 A4-13

where

$$C_1^- = \frac{\sqrt{C_b \gamma_2}}{\sqrt{\gamma_1}\left(\sqrt{\gamma_1} + \sqrt{\gamma_2}\right)}\beta_{app}, \quad C_2^+ = \frac{\sqrt{C_b \gamma_1}}{\sqrt{\gamma_2}\left(\sqrt{\gamma_1} + \sqrt{\gamma_2}\right)}\beta_{app}, \quad A_1 = C_2^+ - C_1^-.$$
(3.29)

For future reference, we compute the leading-order slope of the sheet at the contact line:

$$\tilde{\beta} = \frac{\partial \tilde{g}_0(0, \cdot)}{\partial \tilde{y}} = \frac{\sqrt{\gamma_1}}{\sqrt{\gamma_1} + \sqrt{\gamma_2}}\beta_{app}.$$
(3.30)

This slope is independent of C_b.

We then consider the next-order problem:

$$\dot{a}_0\, \partial_{\tilde{y}}\big(\tilde{h}_0 - \tilde{g}_0\big) + \partial_{\tilde{y}}\big[\big(\tilde{h}_0 - \tilde{g}_0\big)^3 \partial_{\tilde{y}}^3 \tilde{h}_1\big] = 0, \quad 0 < \tilde{y},$$
(3.31a)

$$C_b\, \partial_{\tilde{y}}^4 \tilde{g}_1 - \gamma_1\, \partial_{\tilde{y}\tilde{y}} \tilde{g}_1 = \partial_{\tilde{y}\tilde{y}} \tilde{h}_1, \quad 0 < \tilde{y},$$
(3.31b)

$$C_b\, \partial_{\tilde{y}}^4 \tilde{g}_1 - \gamma_2\, \partial_{\tilde{y}\tilde{y}} \tilde{g}_1 = 0, \quad \tilde{y} < 0.$$
(3.31c)

We integrate (3.31a) for $\tilde{h}_1$ once, and set the constant of integration to zero, to obtain

$$\partial_{\tilde{y}}^3 \tilde{h}_1 = -\frac{\dot{a}_0}{\big(\tilde{h}_0 - \tilde{g}_0\big)^2} = -\frac{\dot{a}_0}{\big(\theta_{app}\tilde{y} + C_1^- - C_1^-\, e^{-\tilde{y}_1}\big)^2}.$$
(3.32)

This equation does not admit a closed-form solution; however, it is possible to find approximate solutions in the far field as $\tilde{y} \to +\infty$, and the near field as $\tilde{y} \to 0$. To find the far-field behaviour, we neglect the exponentially small term on the right-hand side, and consider the far-field approximation $\tilde{h}_1^\infty$ satisfying

$$\partial_{\tilde{y}}^3 \tilde{h}_1^\infty = -\frac{\dot{a}_0}{\theta_{app}^2\, (\tilde{y} + \tilde{c})^2},$$
(3.33)

where the constant is $\tilde{c} = C_1^-/\theta_{app} < 0$. We integrate this equation and use the far-field condition (3.20a) to determine the constant of integration. We obtain

$$\partial_{\tilde{y}} \tilde{h}_1^\infty = -\frac{\alpha_{app}}{a}\tilde{y} + \frac{\dot{a}_0}{\theta_{app}^2}\big\{ \log(\tilde{y} + \tilde{c}) + E_1\big\},$$
(3.34)

where $E_1 = 3 + \log(\epsilon/2a)$.

Similarly, we consider the far-field approximation $\tilde{g}_1^\infty$ for $\tilde{g}_1$, satisfying

$$C_b\, \partial_{\tilde{y}}^4 \tilde{g}_1^\infty - \gamma_1\, \partial_{\tilde{y}\tilde{y}} \tilde{g}_1^\infty = \partial_{\tilde{y}\tilde{y}} \tilde{h}_1^\infty = \frac{\dot{a}_0}{\theta_{app}^2}\frac{1}{\tilde{y} + \tilde{c}} - \frac{\alpha_{app}}{a}.$$
(3.35)

To solve this equation, we integrate it twice and use the far-field condition (3.20b) to determine the constant of integration. We obtain

$$\partial_{\tilde{y}\tilde{y}} \tilde{g}_1^\infty = D_1\, e^{-\tilde{y}_1} - \frac{\beta_{app}}{a} + \frac{1}{\sqrt{\gamma_1 C_b}}\frac{\dot{a}_0}{\theta_{app}^2}\, \varphi\left(\frac{\tilde{y} + \tilde{c}}{l_1}\right),$$
(3.36)

where D_1 is a constant to be determined, and φ is a specific solution to a related second-order ordinary differential equation; see (B3) in Appendix B. We integrate once more to

obtain

$$\partial_{\tilde{y}} \tilde{g}_1^\infty = -D_1 l_1 \, e^{-\tilde{y}_1} - \frac{\beta_{app}}{a} \tilde{y} + \frac{\dot{a}_0}{\gamma_1 \theta_{app}^2} \left\{ \varphi'\left(\frac{\tilde{y} + \tilde{c}}{l_1}\right) - \log(\tilde{y} + \tilde{c}) - E_1 \right\}, \quad (3.37)$$

where the constant of integration is determined by matching to the far-field condition (3.20*b*). We leave the constant D_1 undetermined, as it does not contribute to the far-field behaviour.

So far, we have obtained the far-field behaviour of $\tilde{h}_1$ and $\tilde{g}_1$. We next turn to their near-field behaviour as $\tilde{y} \to 0^+$. To solve (3.32) for $\tilde{h}_1$ in the near field, we first notice from the leading-order solutions (3.25)–(3.28) that $\tilde{h}_0 - \tilde{g}_0$ is analytic in a neighbourhood of $\tilde{y} = 0$. Using a power series to represent the right-hand side of (3.32), we have

$$\partial_{\tilde{y}}^3 \tilde{h}_1 = -\frac{\dot{a}_0}{(\alpha_{app} - \tilde{\beta})^2 \tilde{y}^2} + \mathrm{O}\left(\frac{1}{\tilde{y}}\right), \quad \tilde{y} \to 0^+, \quad (3.38)$$

where the remainder is a power series consisting of terms $\tilde{y}^k$ ($k \geqslant -1$). We perform a term-by-term integration to obtain the near-field approximation

$$\tilde{h}_1^0 = \frac{\dot{a}_0}{(\alpha_{app} - \tilde{\beta})^2}\left(\tilde{y} \log \tilde{y} + \tilde{C}_1 \tilde{y}\right) + \mathrm{O}\left(\tilde{y}^2 \log \tilde{y}, \tilde{y}^2\right), \quad \tilde{y} \to 0^+, \quad (3.39)$$

where $\tilde{C}_1$ is a constant of integration, and the remainder series consists of the terms $\tilde{y}^k$ and $\tilde{y}^k \log \tilde{y}$ ($k \geqslant 2$). We follow a similar procedure and get the equation for $\tilde{g}_1$ near $\tilde{y} = 0$:

$$C_b \, \partial_{\tilde{y}}^4 \tilde{g}_1 - \gamma_1 \, \partial_{\tilde{y}\tilde{y}} \tilde{g}_1 = \frac{\dot{a}_0}{(\alpha_{app} - \tilde{\beta})^2} \frac{1}{\tilde{y}} + \mathrm{O}\left(\log \tilde{y}\right), \quad \tilde{y} \to 0^+. \quad (3.40)$$

We perform a term-by-term integration to obtain the near-field approximation

$$\tilde{g}_1^0 = \frac{\dot{a}_0}{C_b (\alpha_{app} - \tilde{\beta})^2} \tilde{y}^3 \log \tilde{y} + \mathrm{O}\left(\tilde{y}^3, \tilde{y}^4 \log \tilde{y}\right), \quad \tilde{y} \to 0^+, \quad (3.41)$$

where the remainder series consists of terms $\tilde{y}^k$ ($k \geqslant 3$) and $\tilde{y}^k \log \tilde{y}$ ($k \geqslant 4$). In deriving this solution, we have imposed the continuity conditions at the contact line (see the next paragraph) and required matching with the intermediate solution in (3.59) (see § 3.4). Comparing (3.39) and (3.41), we see that $\tilde{h}_1^0$ exhibits a stronger singularity than $\tilde{g}_1^0$.

For $\tilde{y} < 0$, the next-order sheet solution is simply $\tilde{g}_1 \equiv 0$, by noting the far-field condition (3.21) and the continuity conditions (3.22) up to the second derivative at the contact line. To summarise, we have obtained the interface and the sheet solutions up to $\mathrm{O}(\epsilon)$ in the bending region. The leading-order solutions are given in (3.25) and (3.28). The far-field behaviour of the next-order solutions is given in (3.34) and (3.37), while the near-field behaviour is given in (3.39) and (3.41).

3.3. *Inner region*

We now consider the inner region by introducing the rescaled variables $\bar{y} = y/\lambda$, $\bar{h} = h/\lambda$ and $\bar{g} = g/\lambda$. We rewrite the governing equation (3.2) in terms of these inner

variables:

$$\lambda\epsilon \,\partial_t \left(\bar{h} - \bar{g}\right) + \epsilon \dot{a} \,\partial_{\bar{y}} \left(\bar{h} - \bar{g}\right) + \partial_{\bar{y}} \left[\left(\bar{h} - \bar{g}\right)^2 \left(\bar{h} - \bar{g} + 1\right) \partial_{\bar{y}}^3 \bar{h}\right] = 0, \quad 0 < \bar{y}, \quad (3.42a)$$

$$C_b \epsilon^2 \,\partial_{\bar{y}}^4 \bar{g} - \gamma_1 \lambda^2 \,\partial_{\bar{y}\bar{y}} \bar{g} = \lambda^2 \,\partial_{\bar{y}\bar{y}} \bar{h}, \quad 0 < \bar{y}, \quad (3.42b)$$

$$C_b \epsilon^2 \,\partial_{\bar{y}}^4 \bar{g} - \gamma_2 \lambda^2 \,\partial_{\bar{y}\bar{y}} \bar{g} = 0, \quad \bar{y} < 0. \quad (3.42c)$$

At the contact line $\bar{y} = 0$, both the compatibility condition (3.3d) and the continuity conditions in (3.3a) apply. In addition, we impose the contact line conditions (3.3b) and (3.3c). They now become

$$\partial_{\bar{y}} \bar{h} + (\gamma_1 - \gamma_2) \,\partial_{\bar{y}} \bar{g} = -C_b \lambda^{-2} \epsilon^2 \left[\!\left[\partial_{\bar{y}}^3 \bar{g}\right]\!\right], \quad (3.43a)$$

$$\frac{1}{2} \left|\partial_{\bar{y}} \bar{h} - \partial_{\bar{y}} \bar{g}\right|^2 - \frac{1}{2} \theta_Y^2 = \epsilon \mu_\Lambda \dot{a}. \quad (3.43b)$$

We note that since λ is exponentially small compared to ϵ, the equations for $\bar{g}$ reduce to $\partial_{\bar{y}}^4 \bar{g} = 0$, and the contact line condition (3.43a) reduces to $[\![\partial_{\bar{y}}^3 \bar{g}]\!] = 0$. For the purpose of matching, we require the sheet curvature to vanish at infinity, and we obtain the solution

$$\partial_{\bar{y}} \bar{g} \equiv \beta_m = \text{const}, \quad (3.44)$$

which is accurate up to all orders of ϵ.

We only need to expand the interface profile

$$\bar{h}(\bar{y}, t) = \bar{h}_0(\bar{y}, t) + \epsilon \,\bar{h}_1(\bar{y}, t) + \cdots. \quad (3.45)$$

From (3.42a), we see that the leading-order equation for $\bar{h}$ is

$$\partial_{\bar{y}} \left[\left(\bar{h}_0 - \bar{g}_0\right)^2 \left(\bar{h}_0 - \bar{g}_0 + 1\right) \partial_{\bar{y}}^3 \bar{h}_0\right] = 0 \quad \text{for } 0 < \bar{y}, \quad (3.46)$$

and from (3.43b), the leading-order contact line condition is

$$\partial_{\bar{y}} \bar{h}_0 - \partial_{\bar{y}} \bar{g} \equiv \theta_Y \quad \text{at } \bar{y} = 0. \quad (3.47)$$

We further require the interface curvature to vanish at infinity, and hence obtain

$$\partial_{\bar{y}} \bar{h}_0 \equiv \alpha_m = \theta_Y + \beta_m, \quad 0 < \bar{y}. \quad (3.48)$$

For the next-order problem, the governing equation is

$$\dot{a}_0 \,\partial_{\bar{y}} \left(\bar{h}_0 - \bar{g}_0\right) + \partial_{\bar{y}} \left[\left(\bar{h}_0 - \bar{g}_0\right)^2 \left(\bar{h}_0 - \bar{g}_0 + 1\right) \partial_{\bar{y}}^3 \bar{h}_1\right] = 0, \quad 0 < \bar{y}, \quad (3.49)$$

and the contact line condition is

$$\partial_{\bar{y}} \bar{h}_1 = \frac{\mu_\Lambda \dot{a}_0}{\theta_Y} \quad \text{at } \bar{y} = 0. \quad (3.50)$$

We integrate (3.49) and set the constant of integration to zero to obtain

$$\partial_{\bar{y}}^3 \bar{h}_1 = -\frac{\dot{a}_0}{\theta_Y \bar{y} \left(\theta_Y \bar{y} + 1\right)}. \quad (3.51)$$

We integrate further, require the curvature to vanish at infinity, and impose the contact line condition to obtain

$$\partial_{\bar{y}} \bar{h}_1 = \frac{\dot{a}_0}{\theta_Y} \left\{\frac{1}{\theta_Y} \log\left(\theta_Y \bar{y} + 1\right) + \bar{y} \log\left(1 + \frac{1}{\theta_Y \bar{y}}\right) + \mu_\Lambda\right\}. \quad (3.52)$$

From here, we integrate one more time to obtain

$$
\begin{aligned}
\bar{h}_1 &= \frac{\dot{a}_0}{\theta_Y} \left\{ \left(\mu_\Lambda - \frac{1}{2\theta_Y} \right) \bar{y} + \frac{1}{2\theta_Y^2} \log\left(\theta_Y \bar{y} + 1\right) + \frac{1}{\theta_Y} \bar{y} \log\left(\theta_Y \bar{y} + 1\right) \right. \\
&\quad \left. + \frac{1}{2} \bar{y}^2 \left[\log\left(\theta_Y \bar{y} + 1\right) - \log\left(\theta_Y \bar{y}\right) \right] \right\} \\
&\sim \frac{\dot{a}_0}{\theta_Y} \left\{ \frac{1}{\theta_Y} \bar{y} \log \bar{y} + \left(\mu_\Lambda + \frac{\log \theta_Y}{\theta_Y} \right) \bar{y} + \cdots \right\} \quad \text{as } \bar{y} \to +\infty.
\end{aligned}
\tag{3.53}
$$

We note that the inner solutions derived here are valid in an $O(\lambda)$ neighbourhood of the contact line, or when $\bar{y} = O(1)$.

3.4. *Intermediate region*

We proceed to the intermediate region that bridges the inner and bending regions. We apply the transformation

$$
y(s) = \exp\left(\frac{s - 1}{\epsilon} \right), \quad 0 < s < 1 + \epsilon \log \epsilon,
\tag{3.54}
$$

such that $y(0) = \lambda$ corresponds to the inner region, and $y(1 + \epsilon \log \epsilon) = \epsilon$ corresponds to the bending region. Following the usual practice, we also set

$$
h(y(s), t) = H(s, t)\, y, \quad g(y(s), t) = G(s, t)\, y.
\tag{3.55}
$$

These intermediate variables are related to the inner variables via $\bar{y} = e^{s/\epsilon}$, $\bar{h} = H(s, t)\, \bar{y}$ and $\bar{g} = G(s, t)\, \bar{y}$.

To derive the equation for H, we drop the exponentially small term in (3.42a), integrate once, and set the constant of integration to zero. We then rewrite the equation in terms of the intermediate variables to obtain

$$
\epsilon \dot{a} + (H - G)\left(H - G + e^{-s/\epsilon} \right)\left(-\epsilon\, \partial_s H + \epsilon^3\, \partial_s^3 H \right) = 0.
\tag{3.56}
$$

To derive the equation for G, we rewrite (3.42b) in terms of the intermediate variables:

$$
\begin{aligned}
&C_b \epsilon^2\, e^{2(1-s)/\epsilon} \left(2\epsilon\, \partial_s G - \epsilon^2\, \partial_{ss} G - 2\epsilon^3\, \partial_s^3 G + \epsilon^4\, \partial_s^4 G \right) - \gamma_1 \left(\epsilon\, \partial_s G + \epsilon^2\, \partial_{ss} G \right) \\
&= \epsilon\, \partial_s H + \epsilon^2\, \partial_{ss} H.
\end{aligned}
\tag{3.57}
$$

Here we note that when $0 < s < 1 + \epsilon \log \epsilon$, the term $\epsilon^2\, e^{2(1-s)/\epsilon}$ is positive and exponentially large. Therefore, the above equation reduces to

$$
2\, \partial_s G - \epsilon\, \partial_{ss} G - 2\epsilon^2\, \partial_s^3 G + \epsilon^3\, \partial_s^4 G = 0,
\tag{3.58}
$$

with some exponentially small corrections. This equation is linear, independent of H, and can be solved exactly. We obtain $G \equiv \text{const}$ by discarding solutions that lead to an exponentially large curvature. By matching to the inner solution (3.44) and the bending solutions (3.28)–(3.30), we find

$$
G \equiv \beta_m = \tilde{\beta},
\tag{3.59}
$$

which is accurate to all orders of ϵ.

We then turn to solve (3.56). We drop the exponentially small term $e^{-s/\epsilon}$. Since $\partial_s G \equiv 0$, we can rewrite the equation in terms of $H - G$:

$$
\dot{a}_0 + \epsilon \dot{a}_1 - (H - G)^2\, \partial_s\, (H - G) = O\left(\epsilon^2, \epsilon^2 \log \epsilon \right).
\tag{3.60}
$$

From here we solve for $H - G$:

$$(H - G)^3 = (3\dot{a}_0 s + c_0) + \epsilon \left(3\dot{a}_1 s + c_1\right) + O\left(\epsilon^2, \epsilon^2 \log \epsilon\right), \tag{3.61}$$

where c_0 and c_1 are the integration constants to be determined. Further manipulation gives the two-term expansion

$$H - G = (3\dot{a}_0 s + c_0)^{1/3} + \epsilon \frac{3\dot{a}_1 s + c_1}{3 \left(3\dot{a}_0 s + c_0\right)^{2/3}} + O\left(\left(\epsilon \log \epsilon\right)^2\right). \tag{3.62}$$

3.5. *Matching*

The outer and bending solutions have been matched to each other. We now consider the matching between the intermediate and inner solutions. To this end, we rewrite the intermediate solutions (3.62) in terms of the inner variables and expand them in powers of ϵ:

$$\begin{aligned}
\bar{h} - \bar{g} &= (H - G)\,\bar{y} \\
&\sim (3\epsilon \dot{a}_0 \log \bar{y} + c_0)^{1/3}\,\bar{y} + \epsilon \frac{3\epsilon \dot{a}_1 \log \bar{y} + c_1}{3\,(3\epsilon \dot{a}_0 \log \bar{y} + c_0)^{2/3}}\,\bar{y} + \cdots \\
&\sim c_0^{1/3}\bar{y} + \frac{\epsilon}{c_0^{2/3}} \left(\dot{a}_0 \bar{y} \log \bar{y} + \frac{c_1}{3}\bar{y}\right) + \cdots.
\end{aligned} \tag{3.63}$$

This expansion is then matched to the inner solution

$$\bar{h} - \bar{g} \sim \theta_Y \bar{y} + \frac{\epsilon \dot{a}_0}{\theta_Y} \left\{\frac{1}{\theta_Y}\bar{y} \log \bar{y} + \left(\mu_\Lambda + \frac{\log \theta_Y}{\theta_Y}\right)\bar{y}\right\} + \cdots. \tag{3.64}$$

Matching the two expansions term by term, we obtain

$$c_0 = \theta_Y^3, \quad c_1 = 3\dot{a}_0 \left(\mu_\Lambda \theta_Y + \log \theta_Y\right). \tag{3.65}$$

To match the intermediate solutions to the bending ones, we rewrite the intermediate solutions (3.62) in terms of the bending variables and re-expand the expression to get

$$\begin{aligned}
\tilde{h} - \tilde{g} &= (H - G)\,\tilde{y} \\
&\sim (3\dot{a}_0 \left(1 + \epsilon \log \epsilon \tilde{y}\right) + c_0)^{1/3}\,\tilde{y} + \epsilon \frac{3\dot{a}_1 \left(1 + \epsilon \log \epsilon \tilde{y}\right) + c_1}{3\,(3\dot{a}_0 \left(1 + \epsilon \log \epsilon \tilde{y}\right) + c_0)^{2/3}}\,\tilde{y} + \cdots \\
&\sim (c_0 + 3\dot{a}_0)^{1/3}\,\tilde{y} + \frac{\epsilon}{(c_0 + 3\dot{a}_0)^{2/3}} \left\{\dot{a}_0 \tilde{y} \log \tilde{y} + \left(\dot{a}_0 \log \epsilon + \dot{a}_1 + \frac{c_1}{3}\right)\tilde{y}\right\} + \cdots.
\end{aligned} \tag{3.66}$$

This is matched to the near-field bending solution (cf. (3.25)–(3.28), (3.39)–(3.41)):

$$\tilde{h} - \tilde{g} \sim (\alpha_{app} - \tilde{\beta})\tilde{y} + \frac{\epsilon \dot{a}_0}{(\alpha_{app} - \tilde{\beta})^2}(\tilde{y} \log \tilde{y} + \tilde{C}_1 \tilde{y}) + \cdots. \tag{3.67}$$

By matching the corresponding terms, we obtain

$$c_0 + 3\dot{a}_0 = (\alpha_{app} - \tilde{\beta})^3, \quad \frac{\dot{a}_0 \log \epsilon + \dot{a}_1 + c_1/3}{(c_0 + 3\dot{a}_0)^{2/3}} = \frac{\dot{a}_0}{(\alpha_{app} - \tilde{\beta})^2}\tilde{C}_1. \tag{3.68}$$

Combining (3.65) and (3.68), we deduce

$$3\dot{a}_0 = \left(\alpha_{app} - \frac{\sqrt{\gamma_1}}{\sqrt{\gamma_1} + \sqrt{\gamma_2}}\beta_{app}\right)^3 - \theta_Y^3, \qquad (3.69a)$$

$$\dot{a}_1 = \left(\tilde{C}_1 - \mu_\Lambda\theta_Y - \log\theta_Y - \log\epsilon\right)\dot{a}_0, \qquad (3.69b)$$

where we have used (3.30) for the angle $\tilde{\beta}$. Equation (3.69a) provides an estimate for the leading-order contact line speed in terms of the apparent contact angles α_{app} and β_{app}. We note that this equation was derived under the assumption $Ca = \epsilon$; the general case, which can be obtained by a straightforward rescaling of the governing equations, is given in (1.3). Equation (3.69b) gives an estimate for the next-order correction to the contact line speed; however, this correction is of limited practical use, as the constant $\tilde{C}_1$ (cf. (3.39)) remains undetermined. Nevertheless, $\tilde{C}_1$ can, in principle, be determined by solving the full next-order problem in the bending region either analytically or numerically, which we will not consider in this study.

Before concluding this section, we make three remarks concerning (3.69a). First, the relation can be viewed as a generalisation of the classical Cox–Voinov relation. Taking the limit $\gamma_1 \to +\infty$, we find that $\beta_{app} \to 0$ (cf. (3.18)), and we formally recover the classical result

$$3\dot{a}_0 = \theta_{app}^3 - \theta_Y^3. \qquad (3.70)$$

This limiting case corresponds to an infinitely pre-stretched sheet, which excludes any vertical displacement and behaves effectively as a rigid substrate. Second, as long as the friction coefficient μ_Λ is an O(1) parameter, it does not appear in the leading-order relation (3.69a), but only affects the next-order relation (3.69b) through the moving contact line condition applied in the inner region. Finally, (3.69a) is independent of the bending modulus C_b. This is because the slope of the sheet in the bending region near the contact line, $\tilde{\beta}$ (cf. (3.30)), does not depend on C_b. This observation is further supported by the numerical results presented in the next section.

4. Numerical results and discussion

We compare the asymptotic results obtained in the previous section with numerical solutions of the thin-film model. In § 4.1, we show that the interface and sheet profiles, along with their slopes, in the numerical solutions agree well with the asymptotic predictions. In § 4.2, we verify the asymptotic relation (3.69a), and examine the long-time behaviour of the moving contact line in spreading and receding films.

We solve the governing equations (2.18)–(2.20) using a finite difference method with a moving mesh. The numerical method and its validation are detailed in Appendix A. In the simulations, we choose the friction coefficient $\mu_\Lambda = 1$, the equilibrium angle $\theta_Y = 1$, the slip length $\lambda = 10^{-4}$, which corresponds to $\epsilon \approx 0.109$, and the capillary number $Ca = \epsilon$. We vary the parameters γ_1, γ_2 and C_b.

4.1. *Interface and sheet profiles*

We perform the simulations for the spreading and receding dynamics of a liquid film. The parameters in (2.18)–(2.20) are chosen as $\gamma_1 = 2/\epsilon$, $\gamma_2 = 2.95/\epsilon$ and $C_b = \epsilon$. The initial
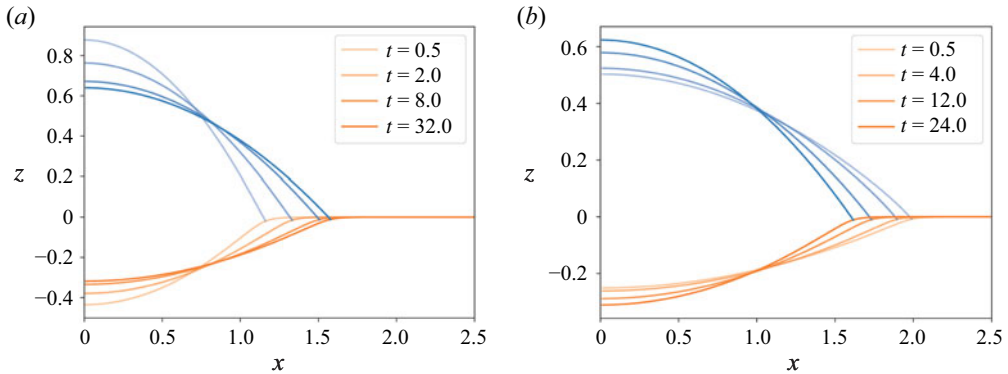
Figure 3. Numerical solutions of the thin-film model (2.18)–(2.20), showing the interface and sheet profiles at different time instants during (*a*) spreading and (*b*) receding dynamics. Blue and orange solid lines denote the interface and sheet, respectively.

interface and sheet profiles are given by

$$h(x, 0) = c_V \left(1 + 0.2 \cos \frac{2\pi x}{a(0)}\right) \left\{1 - \left(\frac{x}{a(0)}\right)^2\right\}, \quad g(x, 0) \equiv 0, \qquad (4.1)$$

where the constant c_V is chosen so that the liquid volume is $V = 1$. We use the initial condition $a(0) = 1.0$ for a spreading film, and $a(0) = 2.0$ for a receding film. In figure 3, we present the simulation results of the interface and sheet profiles at several time instants.

In the spreading case, the contact line advances to the right, the apex heights of both the interface and the sheet decrease, and the liquid film becomes flatter. By $t = 32$, the system has almost reached equilibrium, with the contact line speed dropping below 3×10^{-3}. In the receding case, the contact line retreats to the left, and the liquid becomes more concentrated. By $t = 24$, the system has almost reached equilibrium, with the contact line speed falling below 5×10^{-3}.

Next, we compare the computed interface and sheet profiles at $t = 1$ and $t = 4$ with the asymptotic solutions derived in § 3. The asymptotic solutions invlove the parameters γ_i ($i = 1, 2$), Ca, C_b, θ_Y, μ_Λ, λ, ϵ, and the liquid volume V, together with the apparent contact angles α_{app} and β_{app}, the contact line position $a(t)$, and its velocity components $\dot{a}_0$ and $\dot{a}_1$. All physical parameters (γ_i, Ca, C_b, θ_Y, μ_Λ, λ, ϵ, V) are prescribed in the simulations. The contact line position $a(t)$ at $t = 1, 4$ is obtained directly from the numerical solutions. Given $a(t)$, the apparent contact angles α_{app} and β_{app} are computed using (3.18). The leading-order prediction of the contact line speed $\dot{a}_0$ follows from (3.69*a*). The next-order contact line speed $\dot{a}_1$ cannot be determined directly from (3.69*b*) due to the undetermined constant $\tilde{C}_1$, so we estimate it via $\dot{a}_1 = (\dot{a}_{num} - \dot{a}_0)/\epsilon$, where $\dot{a}_{num}$ is the numerically obtained contact line speed. We note that no parameters or variables are adjusted by fitting in these comparisons.

We first focus on the spreading dynamics discussed above. In figure 4(*a*), the two-term outer solutions $h_0 + \epsilon h_1$ and $g_0 + \epsilon g_1$ from (3.9) and (3.14) are compared with the numerical solutions from the thin-film model at $t = 1.0$ and $t = 4.0$. We observe good overall agreement between the asymptotic and numerical solutions, except that the outer solutions do not capture the smooth bending of the sheet near the contact line. We then examine the bending region. In figure 4(*b*), the leading-order bending solutions $\tilde{h}_0$ and $\tilde{g}_0$, given by (3.25) and (3.28), respectively, are compared with the numerical results.
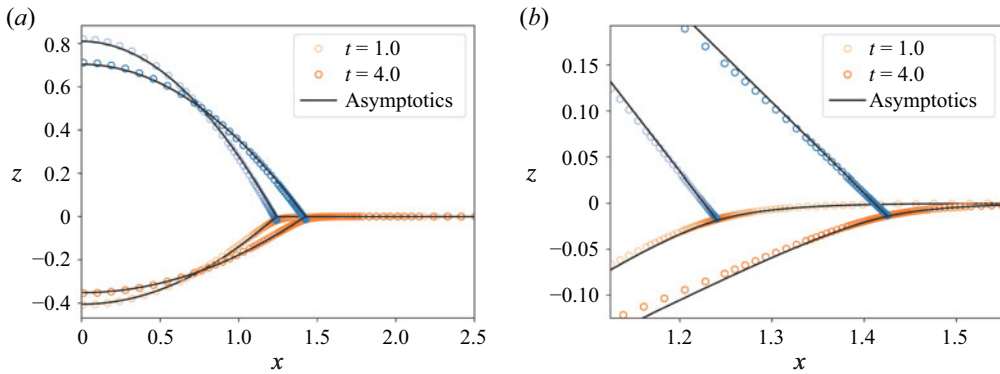
Figure 4. Interface and sheet profiles for a spreading film at $t = 1.0$ and $t = 4.0$, shown in (*a*) the outer region and (*b*) the bending region. Circles denote numerical solutions of the thin-film model (2.18)–(2.20), while solid lines show the asymptotic approximations: the two-term outer solutions from (3.9) and (3.14) in (*a*), and the leading-order bending solutions from (3.25) and (3.28) in (*b*).
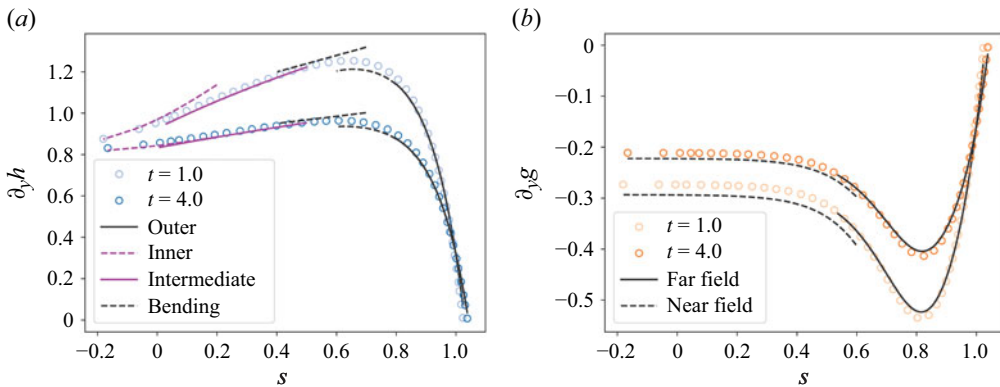

Figure 5. (*a*) Interface slope $\partial_y h$ and (*b*) sheet slope $\partial_y g$ in a spreading film at $t = 1.0$ and $t = 4.0$. Circles denote numerical solutions of the thin-film model (2.18)–(2.20), while lines indicate asymptotic solutions (see text for details). In (*a*), both far-field and near-field bending solutions are shown as black dashed lines, while in (*b*), only the bending region asymptotic solutions are displayed.

These asymptotic solutions agree well with the numerical solutions near the contact line, even though only the leading-order terms are used.

We also compare the numerical and asymptotic solutions in all four regions; in particular, we check the agreement of their slopes. For the same spreading dynamics discussed above, we plot the interface and sheet slopes, $\partial_y h$ and $\partial_y g$, against the intermediate variable $s = \epsilon \log y + 1$ in figures 5(*a*) and 5(*b*), respectively. In figure 5(*a*), we show the interface slopes in their respective regions of validity: (i) the near-field outer solution $\partial_y h_0 + \epsilon \, \partial_y h_1$ from (3.16); (ii) the far-field bending solution $\partial_{\bar{y}} \tilde{h}_0 + \epsilon \, \partial_{\bar{y}} \tilde{h}_1^\infty$ from (3.25) and (3.34); (iii) the near-field bending solution $\partial_{\bar{y}} \tilde{h}_0 + \epsilon \, \partial_{\bar{y}} \tilde{h}_1^0$ from (3.25) and (3.39); (iv) the intermediate solution $H + \epsilon \, H'(s)$ from (3.59) and (3.62); and (v) the inner solution $\partial_{\bar{y}} \bar{h}_0 + \epsilon \, \partial_{\bar{y}} \bar{h}_1$ from (3.48) and (3.53). For the intermediate solution, the next-order contact line speed $\dot{a}_1$ cannot be directly obtained from (3.69*b*), so we estimate it using the numerical contact line speed $\dot{a}_{num}$ via $\dot{a}_1 = (\dot{a}_{num} - \dot{a}_0)/\epsilon$. The two-term bending solution $\tilde{h}_0 + \epsilon \tilde{h}_1^\infty$ is a rearrangement of the outer solution in the bending region (with some higher-order corrections). This explains the smooth connection observed
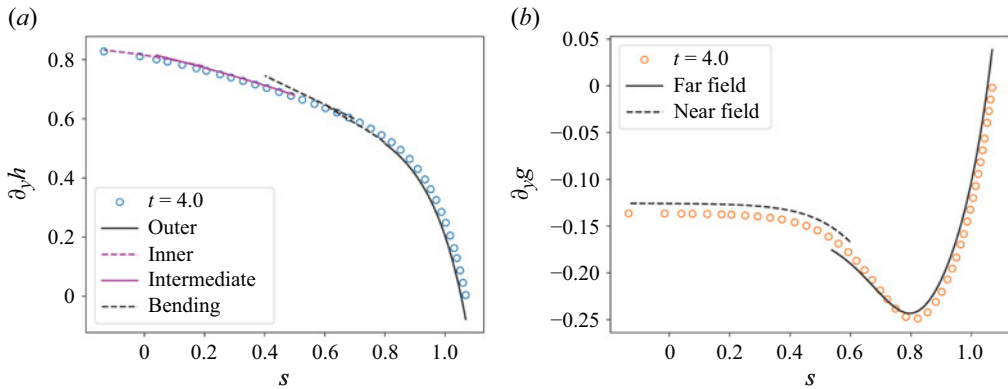
Figure 6. (*a*) Interface slope $\partial_y h$ and (*b*) sheet slope $\partial_y g$ for a receding film at $t = 4.0$. Circles denote numerical solutions of the thin-film model (2.18)–(2.20), while lines indicate asymptotic solutions (see text for details). In (*a*), both far-field and near-field bending solutions are shown as black dashed lines, while in (*b*), only the bending region asymptotic solutions are displayed.

between the outer and bending solutions. Overall, we observe good agreement between the numerical and asymptotic solutions at both $t = 1.0$ and $t = 4.0$. In figure 5(*b*), we overlay the far-field solution $\partial_{\tilde{y}} \tilde{g}_0 + \epsilon \, \partial_{\tilde{y}} \tilde{g}_1^\infty$ (with $D_1 = 0$; cf. (3.37)) and the near-field solution $\partial_{\tilde{y}} \tilde{g}_0 + \epsilon \, \partial_{\tilde{y}} \tilde{g}_1^0$ from (3.28) and (3.41). These asymptotic solutions agree well with the numerical ones in their respective regions of validity. In particular, this validates our prediction of the sheet slope $\tilde{\beta}$ in the bending region, as given in (3.30). The discrepancy towards the inner region is possibly due to the fact that the bending length is not sufficiently small, which limits the accuracy of the asymptotic solution. We also note that the far-field and near-field solutions generally do not match each other near $\tilde{y} = O(1)$, since this lies outside their region of validity.

A similar comparison for the receding film is shown in figures 6(*a*) and 6(*b*). The slope profiles are visually similar at all time instants, so we only present the case $t = 4.0$. Again, we observe good agreement between the numerical results and the asymptotic predictions. We conclude that the asymptotic solutions in all four regions accurately capture the interface and sheet behaviours.

It is interesting to note that the interface does not exhibit a clear bending region. In the numerical solutions, although the bending effect dominates the change in the sheet slope over the interval $s \in (0.5, 0.8)$, the interface slope remains relatively unchanged in the same interval. This indicates that the interface is largely insensitive to small-scale variations in the substrate. We expect similar behaviour in liquid films spreading over substrates with variable height.

4.2. *Contact line motion*

We now compare the contact line speed predicted by the asymptotic relation (3.69*a*) with that obtained from numerical solutions of the thin-film model (2.18)–(2.20). The initial conditions and parameters are the same as in the previous subsection, except that we now vary the tension: $\gamma_1 = 1/\epsilon, 2/\epsilon, 4/\epsilon, 8/\epsilon$ and $\gamma_2 = \gamma_1 + 0.95/\epsilon$. Results for the spreading film and the receding film are shown in figures 7(*a*) and 7(*b*), respectively. Overall, the theoretical predictions agree well with the numerical results, especially for more rigid sheets, i.e. when γ_1 is large. The classical Cox–Voinov relation (3.70) is also shown in the same figures. As γ_1 increases, the results approach the classical one.
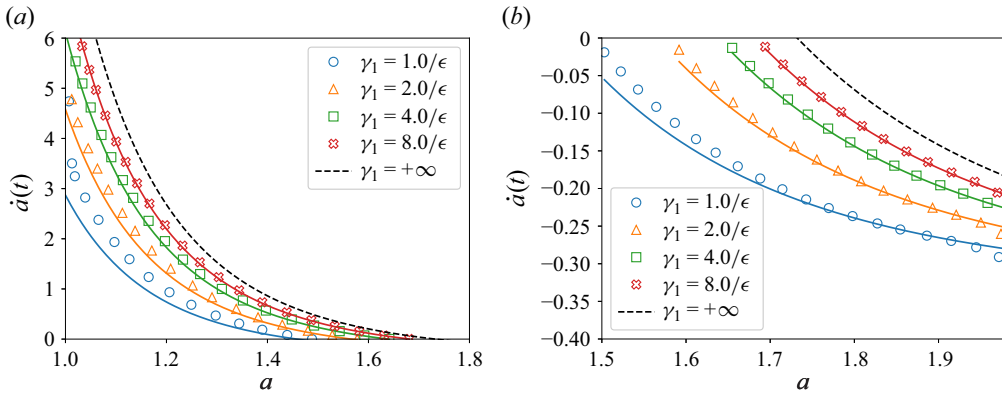
Figure 7. Contact line speed $\dot{a}$ versus film radius $a(t)$ for (a) a spreading film and (b) a receding film. Markers denote numerical solutions of the thin-film model (2.18)–(2.20). Solid lines show predictions from the asymptotic relation (3.69a), while dashed lines are predictions using the classical Cox–Voinov relation (3.70) for rigid substrates.

Another important observation from these figures is that the spreading process becomes slower, and the receding process becomes faster, as the sheet becomes softer. The reason behind this behaviour can be understood from the dependence of the contact angle in the bending region, $\alpha_{app} - \tilde{\beta}$, on the sheet tension. Using (3.18) and (3.30), we can rewrite this angle as

$$\alpha_{app} - \tilde{\beta} = \rho(\gamma_1, \gamma_2)\,\theta_{app}, \tag{4.2a}$$

$$\rho(\gamma_1, \gamma_2) = \frac{1}{1 + \gamma_1^{-1}}\left(1 + \frac{1}{\sqrt{\gamma_1}\left(\sqrt{\gamma_1} + \sqrt{\gamma_2}\right)}\right), \tag{4.2b}$$

where θ_{app} depends only on the volume V and the film radius $a(t)$.

Recall that σ_{pre} is the stretching tension applied to the sheet (cf. (2.1)). When the stretching tension is large, we have

$$\rho = 1 - \frac{1}{2\sigma_{pre}} + O\left(\frac{1}{\sigma_{pre}^2}\right). \tag{4.3}$$

In the limit of a rigid substrate, i.e. as $\sigma_{pre} \to +\infty$, we have $\rho \to 1$, and recover the classical Cox–Voinov relation. For large but finite σ_{pre}, however, $\rho < 1$ and it increases monotonically with σ_{pre}. This reduction in the effective contact angle on softer substrates explains the observed phenomena of retarded spreading and enhanced receding in figures figures 7(a) and 7(b). It is worth noting that the retarded spreading of drops has also been observed on viscoelastic solids (Carré *et al.* 1996; Tamim & Bostwick 2023), where it is mainly attributed to viscous dissipation within the substrate. This mechanism, however, is not relevant here, since purely elastic solids do not exhibit such dissipation.

Next, we examine the effect of the bending modulus C_b on contact line motion. In figure 8, we show numerical results from the thin-film model (2.18)–(2.20) for the contact line speed of a spreading film with $\gamma_1 = 1/\epsilon, 2/\epsilon, 4/\epsilon, 8/\epsilon$ and $C_b = 0.01\epsilon, 0.1\epsilon, \epsilon$. We observe that the speed is barely affected by variations in C_b. Similar behaviour is observed for the receding case (not shown). These results are consistent with the predictions from (3.69a), where the contact line speed is independent of C_b to leading order. We expect the
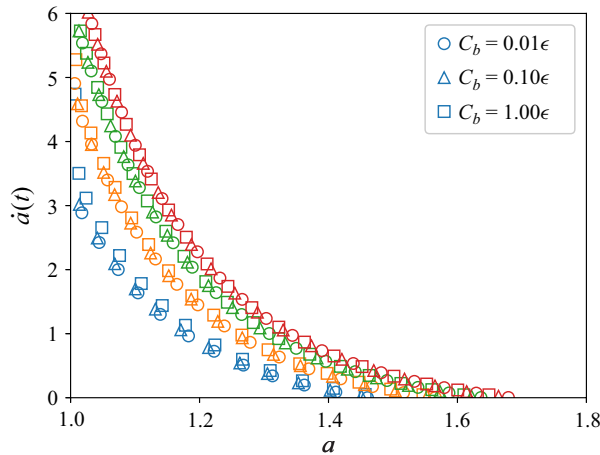
Figure 8. Numerical results from the thin-film model (2.18)–(2.20) for the contact line speed $\dot{a}$ versus the film radius $a(t)$ in a spreading film. Circle, triangle and square markers correspond to $C_b = 0.01\epsilon$, 0.1ϵ and ϵ, respectively. Colours indicate sheet tension: blue for $\gamma_1 = 1/\epsilon$; orange for $\gamma_1 = 2/\epsilon$; green for $\gamma_1 = 4/\epsilon$; and red for $\gamma_1 = 8/\epsilon$.
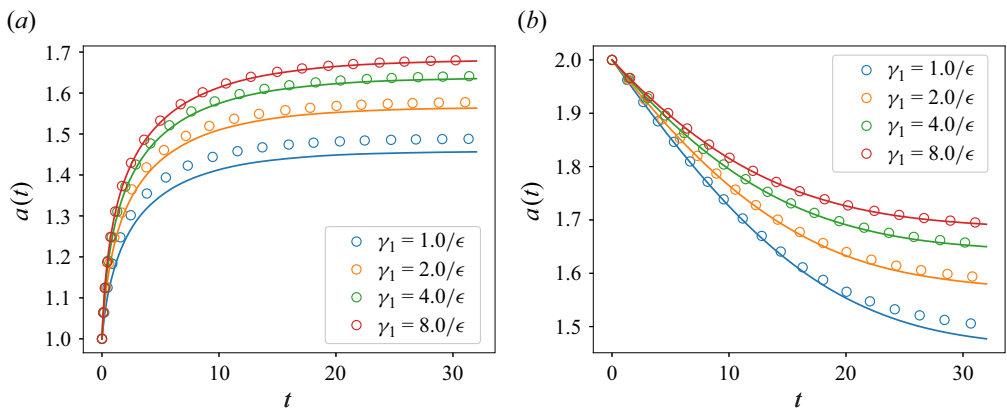

Figure 9. Film radius $a(t)$ for (*a*) a spreading film with $a(0) = 1$, and (*b*) a receding film with $a(0) = 2$, with bending modulus $C_b = \epsilon$. Markers denote numerical solutions of the thin-film model, while solid lines show the leading-order predictions by solving the generalised Cox–Voinov relation (3.69*a*).

relation to remain valid over a wide range of bending moduli, provided that the bending length satisfies $\lambda \ll l_1 \lesssim \epsilon$.

Finally, we plot the film radius against time in figure 9, with $C_b = \epsilon$, varying tensions, and other parameters as prescribed at the beginning of the subsection. In this figure, the markers represent the numerical simulations of the thin-film model, while the solid lines correspond to the predictions from the asymptotic relation (3.69*a*). Here, to get the radius $a(t)$, we solve (3.69*a*) as an ordinary differential equation for a, with its right-hand side rewritten in terms of a using (3.18). Overall, the thin-film dynamics is well captured by the asymptotic relation, particularly for large tensions γ_1. The discrepancies are caused by the facts that the relation (3.69*a*) is only a leading-order approximation, and that the bending length $l_1 = \sqrt{C_b/\gamma_1}$ is not sufficiently small for low values of γ_1. Additionally, the

assumption $\dot{a} \sim \mathrm{O}(1)$ is slightly violated during the initial transient dynamics. The errors accumulated in the transient stage carry over to the later stage of the evolution.

For a liquid film spreading on a rigid substrate, the film radius grows algebraically (Tanner's law) and then approaches its equilibrium value exponentially (Thampi *et al.* 2016). A similar quantitative description can be obtained for the present problem. Let a_∞ denote the equilibrium film radius predicted by (3.69a). By substituting (3.18) and (4.2) into (3.69a), we obtain

$$\dot{a}_0 = 9 \left(\rho(\gamma_1, \gamma_2) \, V \right)^3 \left(a_0^{-6} - a_\infty^{-6} \right). \tag{4.4}$$

At early times when a_0 is far below a_∞, (4.4) can be approximated by

$$\dot{a}_0 \sim 9\rho^3 V^3 a_0^{-6} \quad \Longrightarrow \quad a_0 \sim \left(63\rho^3 V^3 t + a(0) \right)^{1/7}. \tag{4.5}$$

This describes the algebraic regime characterised by the $t^{1/7}$ scaling. The exponent $1/7$ is the same as that in the case of a rigid substrate. At later times, when $\Delta a = a_0 - a_\infty$ is small, (4.4) can be approximated by

$$\frac{\mathrm{d}}{\mathrm{d}t} \Delta a \sim -54\rho^3 V^3 a_\infty^{-7} \, \Delta a \quad \Longrightarrow \quad a_0(t) - a_\infty \sim (a(0) - a_\infty) \exp\left(-54\rho^3 V^3 a_\infty^{-7} t \right). \tag{4.6}$$

This is the exponential regime. Both regimes are quantitatively similar to the spreading on a rigid substrate, and differ in some constants only.

5. Conclusion

We studied the motion of a liquid film on an elastic sheet. We first introduced a thin-film model consisting of fourth-order partial differential equations that couple the dynamics of the fluid interface with the deformation of the elastic sheet, and derived the appropriate contact line conditions following the principles of non-equilibrium thermodynamics.

We then carried out a four-region matched asymptotic analysis on this model in the distinguished limit of small slip length $\lambda \ll 1$, capillary number $Ca = \mathrm{O}(\epsilon)$, and bending length $l = \mathrm{O}(\epsilon)$, where ϵ is given in (1.1). The four regions are: (a) the outer region located at a distance of $\mathrm{O}(1)$ from the contact line, where the apparent contact angles are measured; (b) the bending region of size $\mathrm{O}(l)$ near the contact line where significant sheet bending occurs; (c) the inner region of distance $\mathrm{O}(\lambda)$ from the contact line where fluid slip occurs; and (d) the intermediate region which connects the bending and inner regions. By matching the two-term asymptotic expansions across these regions, we obtained the central result of this study, namely, the generalised Cox–Voinov relation (1.3), which relates the contact line speed to the apparent contact angles. Predictions from this relation show good agreement with numerical solutions of the full thin-film model.

Notable differences in the film motion on an elastic sheet, compared to a rigid substrate, include retarded spreading and enhanced receding. These behaviours are well explained by the generalised Cox–Voinov relation. The increase of the sheet tension (or rigidity) leads to a decrease in the effective contact angle, which alters the contact line dynamics. However, the long-time spreading and receding behaviours, such as those described by Tanner's law, remain quantitatively unchanged. Another interesting aspect of the generalised relation is its independence from the bending length. This suggests that the relation applies to a wide range of bending lengths, which is supported by numerical simulations.

The generalised Cox–Voinov relation (1.3) provides an effective model for the contact line motion in terms of measurable physical quantities, such as the apparent contact angles.

This circumvents the need to resolve microscopic-scale dynamics, as required in the full model. The relation may serve as a useful tool in applications such as coating (Kajiya *et al.* 2014) and inkjet printing (Park & Moon 2006), where control of contact line motion is essential.

Our present analysis is based on the lubrication approximation and is therefore restricted to thin drops with small interfacial slopes. In addition, we have assumed negligible viscosity of the surrounding air and thus ignored its influence on the liquid dynamics. The generalised lubrication formulation (Snoeijer 2006; Chan *et al.* 2020) provides an appealing framework to relax these assumptions. By replacing the classical lubrication equation with this generalised formulation, one should be able to extend the analysis to moving contact lines with large contact angles.

We also expect that the insights and methodology developed in this work can be extended to other soft wetting problems, such as those involving viscoelastic substrates (Kajiya *et al.* 2013, 2014; Karpitschka *et al.* 2015; Kansal *et al.* 2024). To incorporate viscoelastic effects, one must resolve the wetting ridge deformation on the substrate (Jerison *et al.* 2011; Karpitschka *et al.* 2015). This requires identifying the relevant length scale on which the ridge arises, and determining the appropriate distinguished limit. We leave these extensions to future work.

Declaration of interests. The authors report no conflict of interest.

Code availability. The code used in this study is publicly available at https://github.com/zhixuan-zxli/Thin-Film-Code.

Appendix A. Numerical method

We use a moving mesh to handle the moving contact line, and below formulate (2.18) on a moving mesh. Let ξ be the coordinate of a time-independent mesh, and let $x(\xi, t) = a(t)\,\xi$ be the physical coordinate so that the mesh point $\xi = 1$ is always mapped to the contact line. We denote by $\bar{h}$ and $\bar{g}$ the pull-back of h and g onto the time-independent mesh (here, $\bar{h}$ and $\bar{g}$ should not be confused with the inner variables in § 3.3):

$$\bar{h}(\xi, t) = h(x(\xi, t), t), \quad \bar{g}(\xi, t) = g(x(\xi, t), t). \tag{A1}$$

We rewrite the governing equation (2.18) on the time-independent mesh as follows:

$$\partial_t \left(\bar{h} - \bar{g} \right) - \xi \frac{\dot{a}}{a}\, \partial_\xi \bar{h} + \frac{1}{a^4\, Ca} \partial_\xi \left(\left(\bar{h} - \bar{g} \right)^2 \left(\bar{h} - \bar{g} + \lambda \right) \partial_{\xi\xi\xi} \bar{h} \right) = 0, \quad 0 < \xi < 1, \tag{A2a}$$

$$\bar{\kappa} = \frac{1}{a^2}\, \partial_{\xi\xi} \bar{g}, \quad 0 < \xi, \tag{A2b}$$

$$\frac{C_b}{a^2}\, \partial_{\xi\xi} \bar{\kappa} - \gamma_1 \bar{\kappa} = \frac{1}{a^2\, Ca}\, \partial_{\xi\xi} \bar{h}, \quad 0 < \xi < 1, \tag{A2c}$$

$$\frac{C_b}{a^2}\, \partial_{\xi\xi} \bar{\kappa} - \gamma_2 \bar{\kappa} = 0, \quad 1 < \xi, \tag{A2d}$$

where we have introduced the curvature $\kappa = \partial_{xx} g$ and accordingly the pull-back $\bar{\kappa}$ as new unknowns. We note that $\bar{\kappa}$ is continuous across $\xi = 1$, while $\partial_\xi \bar{\kappa}$ has a jump at $\xi = 1$.

For spatial discretisation, we use a bounded domain $[0, \xi_r]$, and discretise $[0, 1]$ into n_f cells, and $[1, \xi_r]$ into $n - n_f$ cells. We use integer subscripts, e.g.

$\xi_1, \dots, \xi_{n_f}, \xi_{n_f+1}, \dots, \xi_n$, to denote the cell centres, and the half subscripts, e.g. $\xi_{(1/2)} = 0, \dots, \xi_{n+(1/2)} = \xi_r$, to denote the cell boundaries. They are related by $\xi_i = (\xi_{i-(1/2)} + \xi_{i+(1/2)})/2$ for $1 \leqslant i \leqslant n$. For temporal discretisation, we use $t^0 = 0, t^1, \dots$ to denote the time instants. The function values at the cell centres are

$$
\begin{aligned}
h_i^m &= \bar{h}(\xi_i, t^m), \quad 1 \leqslant i \leqslant n_f, \ 0 \leqslant m, \\
g_i^m &= \bar{g}(\xi_i, t^m), \quad 1 \leqslant i \leqslant n, \ 0 \leqslant m.
\end{aligned}
\tag{A3}
$$

We use D and D^2 to denote the first- and second-order finite difference operators at the cell centres:

$$
\mathrm{D}h_i = \frac{h_{i+1} - h_{i-1}}{\xi_{i+1} - \xi_{i-1}}, \quad \mathrm{D}^2 h_i = 2 \left(\frac{h_{i+1} - h_i}{\xi_{i+1} - \xi_i} - \frac{h_i - h_{i-1}}{\xi_i - \xi_{i-1}} \right) / (\xi_{i+1} - \xi_{i-1}).
\tag{A4}
$$

We use D^3 to denote the third-order finite difference operator at the cell boundaries,

$$
\mathrm{D}^3 h_{i+\frac{1}{2}} = 3 \frac{\mathrm{D}^2 h_{i+1} - \mathrm{D}^2 h_i}{\xi_{i+2} - \xi_{i-1}}.
\tag{A5}
$$

In addition, we use Δ to denote the forward time difference:

$$
\Delta h^m = \frac{h^{m+1} - h^m}{t^{m+1} - t^m}.
\tag{A6}
$$

Suppose that we have obtained the numerical solutions h^m, g^m, a^m at the time step m. To advance in time, we first update the contact line position according to (2.20c):

$$
Ca \, \mu_\Lambda \, \Delta a^m = \frac{1}{2} \left| \alpha^m - \beta^m \right|^2 - \frac{1}{2} \theta_Y^2,
\tag{A7}
$$

where

$$
\alpha^m = \frac{h_{n_f+1}^m - h_{n_f}^m}{a^m (\xi_{n_f+1} - \xi_{n_f})}, \quad \beta^m = \frac{g_{n_f+1}^m - g_{n_f}^m}{a^m (\xi_{n_f+1} - \xi_{n_f})},
\tag{A8}
$$

are the explicit estimates of (the tangents of) the dynamic contact angles. We then apply a semi-implicit discretisation on (A2a) to obtain

$$
\Delta h_i^m - \Delta g_i^m - \xi_i \frac{\Delta a^m}{a^{m+1}} \left(\mathrm{D}h_i^m - \mathrm{D}g_i^m \right) + \frac{1}{a^{m+1} \, Ca} \frac{F_{i+\frac{1}{2}}^{m+1} - F_{i-\frac{1}{2}}^{m+1}}{\xi_{i+\frac{1}{2}} - \xi_{i-\frac{1}{2}}} = 0, \quad 1 \leqslant i \leqslant n_f,
\tag{A9}
$$

where

$$
F_{i+\frac{1}{2}}^{m+1} = \left(\hat{h}_{i+\frac{1}{2}}^m - \hat{g}_{i+\frac{1}{2}}^m \right)^2 \left(\hat{h}_{i+\frac{1}{2}}^m - \hat{g}_{i+\frac{1}{2}}^m + \lambda \right) \frac{\mathrm{D}^3 h_{i+\frac{1}{2}}^{m+1}}{\left(a^{m+1} \right)^3}
\tag{A10}
$$

is a semi-implicit discretisation of the flux, and $\hat{h}_{i+\frac{1}{2}}$ is the linear interpolation of h_i and h_{i+1} at $\xi_{i+(1/2)}$. For (A2b)–(A2d), we use a fully implicit discretisation:

$$\kappa_i^{m+1} = \frac{D^2 g_i^{m+1}}{\left(a^{m+1}\right)^2}, \quad 1 \leqslant i \leqslant n,$$

$$\frac{C_b}{\left(a^{m+1}\right)^2} \left(D^2 \kappa_i^{m+1} - \eta^{m+1} D^2 v_i^{m+1}\right) - \gamma_1 \kappa_i^{m+1} = \frac{D^2 h_i^{m+1}}{\left(a^{m+1}\right)^2 Ca}, \quad 1 \leqslant i \leqslant n_f, \quad \text{(A11)}$$

$$\frac{C_b}{\left(a^{m+1}\right)^2} \left(D^2 \kappa_i^{m+1} - \eta^{m+1} D^2 v_i^{m+1}\right) - \gamma_2 \kappa_i^{m+1} = 0, \quad n_f + 1 \leqslant i \leqslant n,$$

where $\eta^{m+1} = -[Ca^{-1} \alpha^{m+1} + (\gamma_1 - \gamma_2)\beta^{m+1}]/C_b$ discretises the jump $[\![\partial_x \kappa]\!]$, and

$$v_i^{m+1} = \max \left\{ a^{m+1}\left(\xi_i - 1\right), 0 \right\} \tag{A12}$$

is a correction function for incorporating the jump condition (2.20b) into the finite difference discretisation.

We implement the boundary conditions (2.19) with the help of ghost cells:

$$\begin{aligned} h_0^m &= h_1^m, \quad F_{\frac{1}{2}}^m = 0, \\ g_0^m &= g_1^m, \quad \kappa_0^m = \kappa_1^m, \\ g_n^m + g_{n+1}^m &= 0, \quad \kappa_n^m + \kappa_{n+1}^m = 0. \end{aligned} \tag{A13}$$

At the contact line, we impose

$$F_{n_f+\frac{1}{2}}^m = 0, \quad h_{n_f}^m + h_{n_f+1}^m = g_{n_f}^m + g_{n_f+1}^m. \tag{A14}$$

To validate the numerical method, we perform a series of numerical simulations with successively refined spatial and temporal step sizes. For spatial discretisation, we find $\xi_r = 2$ to be a good cut-off distance for the contact line dynamics to be unaffected. We use a uniform spatial mesh, with $n_f = 128$, $n = 2n_f = 256$ and step size $\Delta \xi = 1/n_f$. For temporal discretisation, we use $t^m = m \, \Delta t$ with $\Delta t = 1/512$. The errors for the temporal and spatial refinement are measured by

$$\begin{aligned} E_{\Delta\xi,\Delta t}[h] &= \max_{1 \leqslant i \leqslant n_f} \left| h_{i,\Delta\xi}^{m,\Delta t} - h_{i,\Delta\xi}^{2m,\Delta t/2} \right|, \\ E_{\Delta\xi,\Delta t}^*[h] &= \max_{1 \leqslant i \leqslant n_f} \left| h_{i,\Delta\xi}^{m,\Delta t} - \frac{1}{2} \left(h_{2i-1,\Delta\xi/2}^{2m,\Delta t/2} + h_{2i,\Delta\xi/2}^{2m,\Delta t/2} \right) \right|, \end{aligned} \tag{A15}$$

with $m = t/\Delta t$, and the final time t to be specified later. The numerical errors for the other unknowns are defined similarly. The parameters used in the refinement tests are $\lambda = 10^{-2}$, $Ca = \epsilon$, $\gamma_1 = 2/\epsilon$, $\gamma_2 = 2.9/\epsilon$, $C_b = \epsilon$ and $\mu_\Lambda = 1$. We confirm the first-order convergence in both time and space, as shown in tables 1 and 2.

For the numerical results presented in §4, where λ was taken to be 10^{-4}, we use a mesh locally refined at the contact line. Specifically, we take mesh size $\Delta \xi = 2^{-i}/32$ in the interval $[1 - 2^{-(i-1)}, 1 - 2^{-i}]$ for $i = 1, 2, \ldots, 9$, and $\Delta \xi_{min} = 2^{-15}$ in the interval $[1 - 2^{-9}, 1]$. Meanwhile, we use adaptive time stepping by starting from $\Delta t = 2^{-19}$, and adjusting it every 128 time steps subject to the CFL-like condition $\Delta t \leqslant \min \{\Delta \xi_{min}/8 \, \Delta a^m, 4 \, \Delta \xi_{min}\}$.

	$E_{\Delta\xi/2,\Delta t/2}$	Rate	$E_{\Delta\xi/2,\Delta t/4}$	Rate	$E_{\Delta\xi/2,\Delta t/8}$
			$t = 0.5$		
$E[h]$	4.70×10^4	1.15	2.11×10^4	1.17	9.37×10^5
$E[g]$	2.33×10^4	1.15	1.05×10^4	1.17	4.64×10^5
$E[\kappa]$	3.83×10^3	1.15	1.73×10^3	1.17	7.70×10^4
$E[a]$	5.89×10^4	1.15	2.65×10^4	1.17	1.17×10^4
	$E_{\Delta\xi/2,\Delta t/2}$	Rate	$E_{\Delta\xi/2,\Delta t/4}$	Rate	$E_{\Delta\xi/2,\Delta t/8}$
			$t = 2.0$		
$E[h]$	7.93×10^5	1.17	3.53×10^5	1.19	1.55×10^5
$E[g]$	3.94×10^5	1.17	1.75×10^5	1.19	7.70×10^6
$E[\kappa]$	4.84×10^4	1.16	2.16×10^4	1.18	9.54×10^5
$E[a]$	1.38×10^4	1.16	6.17×10^5	1.19	2.71×10^5

Table 1. Errors and convergence rates in the time-refinement tests.

	$E^*_{\Delta\xi,\Delta t}$	Rate	$E^*_{\Delta\xi/2,\Delta t/2}$	Rate	$E^*_{\Delta\xi/4,\Delta t/4}$
			$t = 0.5$		
$E^*[h]$	1.03×10^2	0.74	6.18×10^3	0.88	3.36×10^3
$E^*[g]$	5.12×10^3	0.74	3.07×10^3	0.88	1.67×10^3
$E^*[\kappa]$	1.31×10^1	0.74	7.87×10^2	0.86	4.33×10^2
$E^*[a]$	1.43×10^2	0.76	8.43×10^3	0.87	4.62×10^3
	$E^*_{\Delta\xi,\Delta t}$	Rate	$E^*_{\Delta\xi/2,\Delta t/2}$	Rate	$E^*_{\Delta\xi/4,\Delta t/4}$
			$t = 2.0$		
$E^*[h]$	7.07×10^3	0.73	4.25×10^3	0.89	2.29×10^3
$E^*[g]$	3.51×10^3	0.73	2.11×10^3	0.89	1.14×10^3
$E^*[\kappa]$	6.86×10^2	0.77	4.03×10^2	0.88	2.19×10^2
$E^*[a]$	1.34×10^2	0.75	7.99×10^3	0.85	4.42×10^3

Table 2. Errors and convergence rates in the space-refinement tests.

Appendix B. Solution to a second-order ordinary differential equation

Consider the non-homogeneous second-order ordinary differential equation

$$y'' - y = \frac{1}{x} \quad (-\infty < x < +\infty). \tag{B1}$$

The solution is

$$y = C_+ e^x + C_- e^{-x} + \varphi(x), \tag{B2}$$

where C_+ and C_- are constants of integration depending on initial or boundary conditions. The specific solution is

$$\varphi(x) = \frac{1}{2} \left[e^x \, \text{Ei}\,(-x) - e^{-x} \, \text{Ei}\,(x) \right], \tag{B3}$$

where

$$\text{Ei}(x) = \int_{-\infty}^{x} \frac{e^t}{t} \, dt \tag{B4}$$

is the exponential integral. The derivatives of the specific solution satisfy

$$\varphi' = \frac{1}{2} \left[e^x \, \mathrm{Ei}(-x) + e^{-x} \, \mathrm{Ei}(x) \right],$$
$$\varphi'' = \frac{1}{2} \left[e^x \, \mathrm{Ei}(-x) - e^{-x} \, \mathrm{Ei}(x) \right] + \frac{1}{x} = \varphi + \frac{1}{x}. \tag{B5}$$

There are two asymptotic series for the exponential integral (O'Malley 2014),

$$\mathrm{Ei}(x) \sim \log|x| + \gamma_E + e^{x/2} \left(x - \frac{1}{4}x^2 + \cdots \right), \quad x \to 0,$$
$$\mathrm{Ei}(x) \sim \frac{e^x}{x} \left(\sum_{k=0} \frac{k!}{x^k} + \cdots \right), \quad |x| \to \infty, \tag{B6}$$

for small x and large x, respectively. Here, $\gamma_E \approx 0.57722$ is Euler's constant. From these series, we have the following asymptotic expansions for the specific solution:

$$\varphi \sim x \log|x| + (\gamma_E - 1)\, x, \quad \varphi' \sim \gamma_E + \log|x| \quad \text{as } x \to 0,$$
$$\varphi \sim -\frac{1}{x}, \quad \varphi' \sim \frac{1}{x^2} \quad \text{as } |x| \to \infty. \tag{B7}$$

REFERENCES

ANDREOTTI, B. & SNOEIJER, J.H. 2020 Statics and dynamics of soft wetting. *Annu. Rev. Fluid Mech.* **52** (1), 285–308.

BICO, J., REYSSAT, E. & ROMAN, B. 2018 Elastocapillarity: when surface tension deforms elastic solids. *Annu. Rev. Fluid Mech.* **50** (1), 629–659.

BONN, D., EGGERS, J., INDEKEU, J., MEUNIER, J. & ROLLEY, E. 2009 Wetting and spreading. *Rev. Mod. Phys.* **81** (2), 739–805.

BRADLEY, A.T., BOX, F., HEWITT, I.J. & VELLA, D. 2019 Wettability-independent droplet transport by bendotaxis. *Phys. Rev. Lett.* **122** (7), 074503.

BRUBAKER, N.D. & LEGA, J. 2015 Two-dimensional capillary origami with pinned contact line. *Siam J. Appl. Math.* **75** (3), 1275–1300.

CARRÉ, A., GASTEL, J.-C. & SHANAHAN, M.E.R. 1996 Viscoelastic effects in the spreading of liquids. *Nature* **379** (6564), 432–434.

CHAN, T.S., KAMAL, C., SNOEIJER, J.H., SPRITTLES, J.E. & EGGERS, J. 2020 Cox–Voinov theory with slip. *J. Fluid Mech.* **900**, A8.

CHARITATOS, V. & KUMAR, S. 2020 A thin-film model for droplet spreading on soft solid substrates. *Soft Matter* **16** (35), 8284–8298.

COX, R.G. 1986 The dynamics of the spreading of liquids on a solid surface. Part 1. Viscous flow. *J. Fluid Mech.* **168** (1), 169.

DAVIDOVITCH, B., SCHROLL, R.D., VELLA, D., ADDA-BEDIA, M. & CERDA, E.A. 2011 Prototypical model for tensional wrinkling in thin sheets. *Proc. Natl Acad. Sci.* **108** (45), 18227–18232.

DAVIDOVITCH, B. & VELLA, D. 2018 Partial wetting of thin solid sheets under tension. *Soft Matter* **14** (24), 4913–4934.

DE GENNES, P.G. 1985 Wetting: statics and dynamics. *Rev. Mod. Phys.* **57** (3), 827–863.

EHRHARD, P. & DAVIS, S.H. 1991 Non-isothermal spreading of liquid drops on horizontal plates. *J. Fluid Mech.* **229** (1), 365.

HENKEL, C., SNOEIJER, J.H. & THIELE, U. 2021 Gradient-dynamics model for liquid drops on elastic substrates. *Soft Matter* **17** (45), 10359–10375.

HOCKING, L.M. 1977 A moving fluid interface. Part 2. The removal of the force singularity by a slip flow. *J. Fluid Mech.* **79** (2), 209–229.

HOCKING, L.M. 1983 The spreading of a thin drop by gravity and capillarity. *Q. J. Mech. Appl. Maths* **36** (1), 55–69.

HOCKING, L.M. & RIVERS, A.D. 1982 The spreading of a drop by capillary action. *J. Fluid Mech.* **121** (1), 425.

HUANG, J., JUSZKIEWICZ, M., DE JEU, W.H., CERDA, E., EMRICK, T., MENON, N. & RUSSELL, T.P. 2007 Capillary wrinkling of floating thin polymer films. *Science* **317** (5838), 650–653.

HUH, C. & SCRIVEN, L. 1971 Hydrodynamic model of steady movement of a solid/liquid/fluid contact line. *J. Colloid Interface Sci.* **35** (1), 85–101.

JERISON, E.R., XU, Y., WILEN, L.A. & DUFRESNE, E.R. 2011 Deformation of an elastic substrate by a three-phase contact line. *Phys. Rev. Lett.* **106** (18), 186103.

KAJIYA, T., BRUNET, P., ROYON, L., DAERR, A., RECEVEUR, M. & LIMAT, L. 2014 A liquid contact line receding on a soft gel surface: dip-coating geometry investigation. *Soft Matter* **10** (44), 8888–8895.

KAJIYA, T., DAERR, A., NARITA, T., ROYON, L., LEQUEUX, F. & LIMAT, L. 2013 Advancing liquid contact line on visco-elastic gel substrates: stick-slip vs. continuous motions. *Soft Matter* **9** (2), 454–461.

KAMAL, C., SPRITTLES, J.E., SNOEIJER, J.H. & EGGERS, J. 2019 Dynamic drying transition via free-surface cusps. *J. Fluid Mech.* **858**, 760–786.

KANSAL, M., BERTIN, V., DATT, C., EGGERS, J. & SNOEIJER, J.H. 2024 Viscoelastic wetting: Cox–Voinov theory with normal stress effects. *J. Fluid Mech.* **985**, A17.

KARPITSCHKA, S., DAS, S., VAN GORCUM, M., PERRIN, H., ANDREOTTI, B. & SNOEIJER, J.H. 2015 Droplets move over viscoelastic substrates by surfing a ridge. *Nat. Commun.* **6** (1), 7891.

KING, H., SCHROLL, R.D., DAVIDOVITCH, B. & MENON, N. 2012 Elastic sheet on a liquid drop reveals wrinkling and crumpling as distinct symmetry-breaking instabilities. *Proc. Natl Acad. Sci.* **109** (25), 9716–9720.

LI, Z. & REN, W. 2024a Relaxation dynamics of capillary folding of thin elastic sheets with pinned contact lines. *J. Fluid Mech.* **978**, A31.

LI, Z. & REN, W. 2024b Simulating capillary folding of thin elastic sheets with pinned contact lines. *J. Comput. Phys.* **511**, 113124.

NGAN, C.G. & DUSSAN, E.B.V. 1989 On the dynamics of liquid spreading on solid surfaces. *J. Fluid Mech.* **209**, 191–226.

ORON, A., DAVIS, S.H. & BANKOFF, S.G. 1997 Long-scale evolution of thin liquid films. *Rev. Mod. Phys.* **69** (3), 931–980.

O'MALLEY, R.E. 2014 *Asymptotic Approximations*. Springer International Publishing.

PANDEY, A., ANDREOTTI, B., KARPITSCHKA, S., VAN ZWIETEN, G.J., VAN BRUMMELEN, E.H. & SNOEIJER, J.H. 2020 Singular nature of the elastocapillary ridge. *Phys. Rev. X* **10** (3), 031067.

PARK, J. & MOON, J. 2006 Control of colloidal particle deposit patterns within picoliter droplets ejected by ink-jet printing. *Langmuir* **22** (8), 3506–3513.

PY, C., REVERDY, P., DOPPLER, L., BICO, J., ROMAN, B. & BAROUD, C.N. 2007 Capillary origami: spontaneous wrapping of a droplet with an elastic sheet. *Phys. Rev. Lett.* **98** (15), 156103.

PÉRAUD, J.-P. & LAUGA, E. 2014 Geometry and wetting of capillary folding. *Phys. Rev. E* **89** (4), 043011.

REN, W. & E., W. 2007 Boundary conditions for the moving contact line problem. *Phys. Fluids* **19** (2), 022101.

REN, W. & E., W. 2011 Derivation of continuum models for the moving contact line problem based on thermodynamic principles. *Commun. Math. Sci.* **9** (2), 597–606.

REN, W., HU, D. & E., W. 2010 Continuum models for the contact line problem. *Phys. Fluids* **22** (10), 102103.

REN, W., TRINH, P.H. & E., W. 2015 On the distinguished limits of the Navier slip model of the moving contact line problem. *J. Fluid Mech.* **772**, 107–126.

SAVVA, N. & KALLIADASIS, S. 2009 Two-dimensional droplet spreading over topographical substrates. *Phys. Fluids* **21** (9), 092102.

SCHROLL, R.D., ADDA-BEDIA, M., CERDA, E., HUANG, J., MENON, N., RUSSELL, T.P., TOGA, K.B., VELLA, D. & DAVIDOVITCH, B. 2013 Capillary deformations of bendable films. *Phys. Rev. Lett.* **111** (1), 014301.

SHANAHAN, M.E.R. 1988 The spreading dynamics of a liquid drop on a viscoelastic solid. *J. Phys. D: Appl. Phys.* **21** (6), 981–985.

SIBLEY, D.N., NOLD, A. & KALLIADASIS, S. 2015 The asymptotics of the moving contact line: cracking an old nut. *J. Fluid Mech.* **764**, 445–462.

SNOEIJER, J.H. 2006 Free-surface flows with large slopes: beyond lubrication theory. *Phys. Fluids* **18** (2), 021701.

SNOEIJER, J.H. & ANDREOTTI, B. 2013 Moving contact lines: scales, regimes, and dynamical transitions. *Annu. Rev. Fluid Mech.* **45** (1), 269–292.

STONE, H., STROOCK, A. & AJDARI, A. 2004 Engineering flows in small devices: microfluidics toward a lab-on-a-chip. *Annu. Rev. Fluid Mech.* **36** (1), 381–411.

STYLE, R.W. & DUFRESNE, E.R. 2012 Static wetting on deformable substrates, from liquids to soft solids. *Soft Matter* **8** (27), 7177.

TAMIM, S. & BOSTWICK, J.B. 2023 Spreading of a thin droplet on a soft substrate. *J. Fluid Mech.* **971**, A32.

TAMIM, S.I. & BOSTWICK, J.B. 2021 Model of spontaneous droplet transport on a soft viscoelastic substrate with nonuniform thickness. *Phys. Rev. E* **104** (3), 034611.

TANGPARITKUL, S., CHARPENTIER, T., PRADILLA, D. & HARBOTTLE, D. 2018 Interfacial and colloidal forces governing oil droplet displacement: implications for enhanced oil recovery. *Colloids and Interfaces* **2** (3), 30.

THAMPI, S.P., PAGONABARRAGA, I., ADHIKARI, R. & GOVINDARAJAN, R. 2016 Universal evolution of a viscous–capillary spreading drop. *Soft Matter* **12**, 6073–6078.

VOINOV, O.V. 1977 Hydrodynamics of wetting. *Fluid Dyn.* **11** (5), 714–721.

YAO, J., ZHANG, Z. & REN, W. 2023 Modelling moving contact lines on inextensible elastic sheets in two dimensions. *J. Fluid Mech.* **955**, A25.

YOUNG, T. 1805 III. An essay on the cohesion of fluids. *Phil. Trans. R. Soc. Lond.* **95**, 65–87.

ZHANG, Z. & QIAN, T. 2022 Variational approach to droplet transport via bendotaxis: thin film dynamics and model reduction. *Phys. Rev. Fluids* **7** (4), 044002.

ZHANG, Z., YAO, J. & REN, W. 2020 Static interface profiles for contact lines on an elastic membrane with the willmore energy. *Phys. Rev. E* **102** (6), 062803.